Longitudinal Fluctuations in Ultra-Relativistic Heavy-Ion Collisions

A Thesis

submitted to
Indian Institute of Science Education and Research Pune
in partial fulfillment of the requirements for the
BS-MS Dual Degree Programme

by

Sruthy J. Das

Indian Institute of Science Education and Research Pune
Dr. Homi Bhabha Road,
Pashan, Pune 411008, INDIA.

April, 2019

Supervisor: Prof. Rajeev S. Bhalerao
Co-supervisor: Prof. Jean-Yves Ollitrault

Certificate

This is to certify that this dissertation entitled **Longitudinal Fluctuations in Ultra-Relativistic Heavy-Ion Collisions** towards the partial fulfilment of the BS-MS dual degree programme at the Indian Institute of Science Education and Research, Pune represents study/work carried out by Sruthy J. Das at Indian Institute of Science Education and Research under the joint supervision of Prof. Jean-Yves Ollitrault, IPhT, CEA Saclay, France and myself, during the academic year 2018-2019.

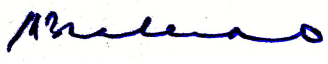

Prof. Rajeev S. Bhalerao

Raja Ramanna Fellow

Department of Physics

IISER Pune

Committee:

Prof. Rajeev S. Bhalerao

Prof. Sourabh Dube

This thesis is dedicated to my mother, Jyothi.

Declaration

I hereby declare that the matter embodied in the report entitled **Longitudinal Fluctuations in Ultra-Relativistic Heavy-Ion Collisions** are the results of the work carried out by me at the Department of Physics, Indian Institute of Science Education and Research, Pune, under the supervision of Prof. Rajeev S. Bhalerao and Prof. Jean-Yves Ollitrault, and the same has not been submitted elsewhere for any other degree.

Sruthy J. Das

Acknowledgments

I would like to sincerely thank my project supervisor Prof. Rajeev S. Bhalerao for his constant support and guidance throughout this journey. I also thank him for providing me the opportunity to meet world-experts in the field like Prof. Jean-Yves Ollitrault, Prof. Ulrich Heinz, Prof. Matthew Luzum and Prof. Jamie Nagle. I especially thank Prof. Jean-Yves Ollitrault for valuable inputs in developing the project and constant support. I also thank Giuliano Giacalone and Chandrodoy Chattopadhyay for the valuable discussions. I am also grateful to Prof. Sourabh Dube for helpful discussions and support. I would like to thank Nisha Kurkure for helping me with the computer programming. I acknowledge the financial support from Infosys Foundation Scholarship.

I am much grateful to Prof. Seema Sharma for the support and encouragement. I specially thank Sravya Pamula, Nishant Raina and Steenu Johnson for accompanying in coffee time. Also, Goutham Sukumaran and Namithasree, thank you for being in my life. Finally, I thank my parents and my sister for the constant love and encouragement.

Abstract

In this thesis we focus on understanding the longitudinal fluctuations in the initial state of relativistic nuclear collisions when Quark-Gluon Plasma is formed. Hydrodynamic evolution of the QGP state is performed using the three-dimensional viscous hydrodynamic code $MUSIC$ with fluctuating initial density profiles generated using T_RENTo 3D of Pb+Pb collisions at $\sqrt{s_{NN}} = 5.02$ TeV in the centrality range 0 to 1%. The initial state fluctuations leave their signature on the emitted particles as flow coefficients. Anisotropic flows of the emitted particles are analyzed in order to study the fluctuations in the system. Two-particle correlation matrices corresponding to the multiplicity fluctuation, elliptic and triangular flow are constructed and analyzed through the statistical technique called principal component analysis. This method reveals the leading and the sub-leading modes of the fluctuations in the longitudinal direction. The non-flow effects in the flow coefficients are reduced by introducing gaps in the pseudorapidity bins while constructing the two-particle correlation matrix. Longitudinal decorrelations in terms of flow vector, flow magnitude and flow orientation are also explored. Sub-leading modes in pseudorapidity are clearly visible and measurable even after imposing a sizable gap.

Contents

List of Tables

List of Figures

Chapter 1

Introduction

Quark-Gluon Plasma (QGP) is a strongly-coupled state of matter created in relativistic nuclear collisions in the form of microscopic droplets. The myriad of particles that are formed from this droplet tell us about the properties of QGP. Computational models have been developed which precisely enact the entire process, starting from generating the initial density profile at the thermalization time of QGP, followed by its hydrodynamic evolution, subsequent particlization and finally computing particle observables. Analyzing particle observables of interest through statistical procedures reveals underlying properties of this strongly coupled matter.

1.1 A historical overview of heavy-ion collisions

In the past twenty years, the relativistic heavy-ion collision experiments conducted at the Relativistic Heavy-Ion Collider (RHIC) and Large Hadron Collider (LHC) have been successful in creating strongly-interacting high-density nuclear matter through nucleus-nucleus and proton-nucleus collisions. An interesting feature is that this short-lived state behaves like an almost perfect liquid droplet with very small viscosity, and has been called strongly-interacting Quark-Gluon Plasma (sQGP). It eventually hadronizes into different kinds of particles. Initial expectations were of a gas-like system of weakly interacting particles (wQGP), expanding almost isotropically because of the extreme high density achieved in heavy-ion collisions. But the first results at RHIC showed otherwise.

Significant azimuthal anisotropy was observed in the distribution of particles emerging out of the heavy-ion collision [1].

1.2 Dynamical evolution of a HIC event

Figure. (1.1) displays timeline of a typical heavy-ion collision event. Large nuclei such as Pb or Au have a diameter of about 14 fm. Since the collision is happening at relativistic energies (2.76 TeV or 5.02 TeV) the colliding nuclei are Lorentz-contracted and are in the form of discs. As a consequence, it creates a very high energy density right after the two nuclei collide. Most of the collisions involve little momentum transfer since only a small fraction of the discs overlap. The system is quite far from equilibrium initially. The quarks and gluons formed as a result of the collision are not independent of each other. They are very strongly correlated and the state has been named Quark-Gluon Plasma (QGP). It has now been established that the evolution of this strongly-correlated matter until the formation of particles can be modelled using relativistic viscous fluid dynamics. The data agreed quite well with the initial calculations using ideal hydrodynamics. Later on, improved agreements have been achieved with viscous hydrodynamics with very small shear viscosity to entropy density ratio, $\eta/s \approx 1/4\pi$. Sometime after the collision, the pressure-driven hydrodynamic expansion causes the dense matter to develop a flow in the plane that is perpendicular to the beam axis. This is usually called the transverse flow. In the final stages of the collision, consisting of a dilute system of hadrons, hydrodynamical approach cannot be used since the system is far from equilibrium.

It is still not completely understood how a strongly interacting system attains thermal equilibrium in a time $\tau_0 < 1$ fm/c. Typically, critical temperature, T_c is 155-160 MeV. Below this temperature, quarks and gluons in QGP combine to form hadrons. The cross-over between QGP and hadrons is shown in Fig. (1.2). Inelastic reactions between different species of hadrons cease at a temperature $\approx 165MeV$ corresponding to $\tau \approx 10fm$. This stage is called chemical freezeout. After the chemical freezeout the relative number of stable hadrons remains constant. Generally the fluid will continue evolving till a kinetic freeze out occurs. Kinetic freezeout temperature is defined as the temperature at which even elastic scatterings stop. This occurs at a temperature $\approx 120MeV$ corresponding to $\tau \approx 15fm$. Subsequently, the hadrons continue free-streaming towards the detector and hadronic

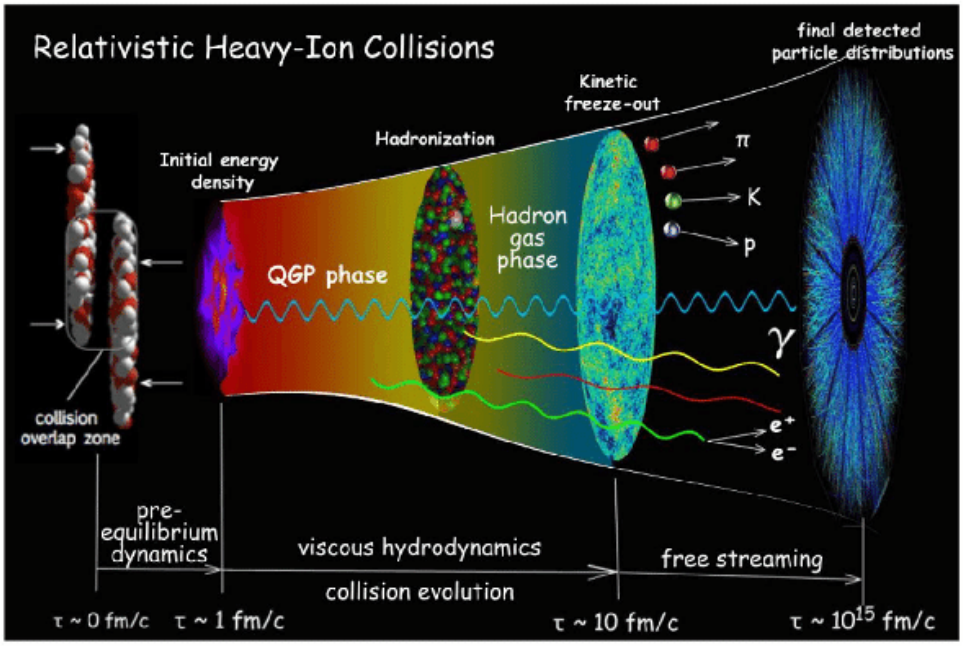

Figure 1.1: Illustration of time evolution of heavy-ion collision [2].

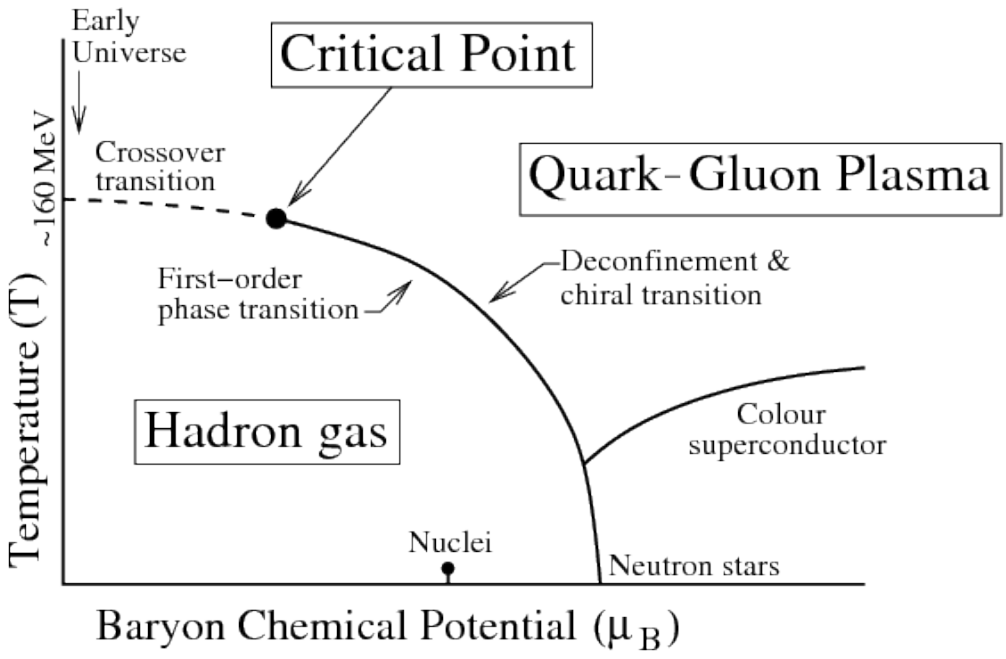

Figure 1.2: QCD Phase Diagram.

observables are studied.

1.3 Development of Anisotropies

The heavy-ion collision is very fast and has a high expansion rate. So the system never achieves a global thermal equilibrium. It is observed that the fluctuation in the initial state leaves its signature on the final-state particle observables rather than dying out [3]. Because of the geometry of the overlapping region of colliding nuclei, anisotropic pressure gradients develop and result in the anisotropic distribution of final particles. Analyzing the anisotropic flow reveals information about the initial state of the system. This thesis aims to gather valuable information about pseudorapidity dependence of flow fluctuations.

1.4 Outline

In this thesis, I discuss the pseudorapidity dependence of longitudinal fluctuations by analyzing anisotropic flow through a statistical procedure called principal component analysis (PCA). The major goal is to study the properties of the initial state of nuclear collision when strongly interacting Quark-Gluon Plasma (QGP) is formed.

Historical introduction has been provided in this chapter. In chapter 2, we discuss the different stages of heavy-ion collision by introducing simulation models with detailed explanations. Different kinds of interesting hadronic observables including the two-particle correlation matrix which can provide information about the initial state of heavy-ion collisions are discussed in chapter 3. In chapter 4, I describe in depth the construction of the correlation matrix and how PCA reveals information about fluctuations in the anisotropic flow coefficients from the correlation matrix. Chapter 5 discusses a technique which reduces the contribution of short-range nonflow effects present in the correlation matrix. In chapter 6, some additional properties of the longitudinal fluctuations in the system are discussed. Finally, we present the most important conclusions in chapter 7.

Chapter 2

Modelling of heavy-ion collisions

2.1 Initial density model T_RENTo

Dynamic initial-condition models simulate an initial profile with the preequilibrium evolution dynamics. For our purposes, we are using a nondynamic initial-condition model called T_RENTo which generates initial energy density or entropy density profile at the thermalization time of the strongly coupled QGP which is later evolved using hydrodynamical models [4]. T_RENTo does not simulate any preequilibrium evolution.

It generates the initial density profile at the thermalization time by constructing a thickness function for each projectile. The participant thickness function is defined as

$$T_{A,B}(x,y) = \int dz \rho_{A,B}(x,y,z), \tag{2.1}$$

where A and B denote projectiles colliding along the z axis and ρ is the participant nuclear density. When the target and projectile nuclei overlap, it is assumed that entropy is produced. In reality, the initial density profile fluctuates from one collision event to another. So in the thickness function, an independent random weight denoted by $w_{A,B}$ is introduced.

$$T_{A,B}(x,y) = w_{A,B} \int dz \rho_{A,B}(x,y,z) \tag{2.2}$$

A scalar function f is constructed which converts the thickness function into entropy deposition.

$$f \propto \frac{dS}{dy}\Big|_{\tau=\tau_0}, \tag{2.3}$$

where $\frac{dS}{dy}$ is the entropy density at midrapidity. The scalar function f is constructed as

$$f = T_R(p; T_A, T_B) \equiv \left(\frac{T_A^p + T_B^p}{2}\right)^{1/p}. \tag{2.4}$$

Depending on the value of p, the scalar function called generalised mean oscillates between the minimum and maximum of T_A and T_B. We are using $p = 0$ which corresponds to geometric mean where there is a symmetric entropy deposition at the midrapidity.

T_RENTo is a modified version of Monte Carlo Glauber model developed by PHOBOS collaboration. In this model, nuclear charge density distribution is parameterized as

$$e(r) = e_0 \frac{1 + w(\frac{r}{R})^2}{1 + \exp{(\frac{r-R}{a})}}. \tag{2.5}$$

In this equation, e_0 is the normalization constant and the parameters w, R and a define the shape of the nucleus. The variable $r = \sqrt{x^2 + y^2}$ denotes a point in the transverse plane inside the nucleus. Let us consider a Pb-Pb collision. When we simulate an event, a random impact parameter, b, which ranges from 0 to 20 fm approximately, is generated based on the probability distribution $\frac{dN}{db} \propto b$. The number of nucleons interacting in a collision event is called the number of participant nucleons, N_p. For Pb-Pb collision, the upper limit of N_p is 416. The distribution of participant nucleons in the transverse plane is important for hydrodynamics, because these interaction points are the sources of energy or entropy density after the collision.

2.1.1 Centrality cuts

Centrality is an important quantity to sort and categorize the fluctuating events based on their charged hadron multiplicity at mid-rapidity, $dN^{ch}/d\eta|_{|\eta|<0.5}$. The total initial entropy

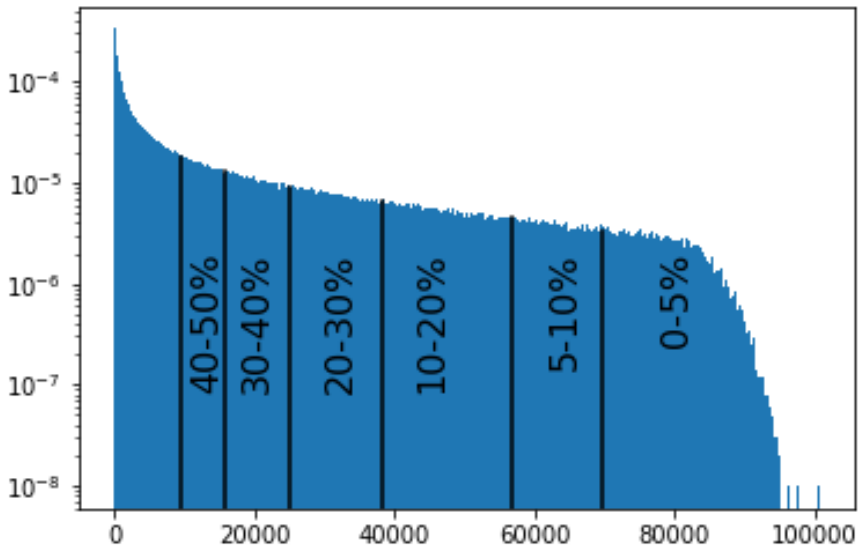

Figure 2.1: Histogram of total initial entropy dS/dy using 1 million events generated from T_RENTo.

in the transverse plane is linear in relation with the charged hadron multiplicity.

$$\left.\frac{dS}{dy}\right|_{y=0} \propto \left.\frac{dN^{ch}}{d\eta}\right|_{|\eta|<0.5}. \tag{2.6}$$

The correct total initial entropy in the transverse plane is fixed by matching the charged hadron multiplicity to the experimental data. So events can be sorted out based on the total initial entropy in the transverse plane. When the two colliding nuclei completely overlap, the charged hadron multiplicity will also be maximum and it is called a central collision. The 0-1% central collisions consists of 1% of all the collision events with the largest $dS/dy|_{y=0}$. The classification of events based on centrality is shown in Fig. (2.1).

2.1.2 Fluctuation in three dimension

In reality, every collision event differs from another in the distribution of lumps of initial energy density in the three dimensions i.e., x, y and η. T_RENTo 3D is a three-dimensional

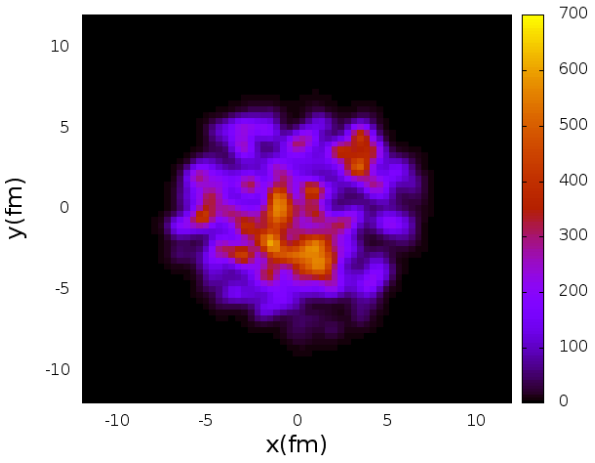

Figure 2.2: Fluctuation in the xy plane.

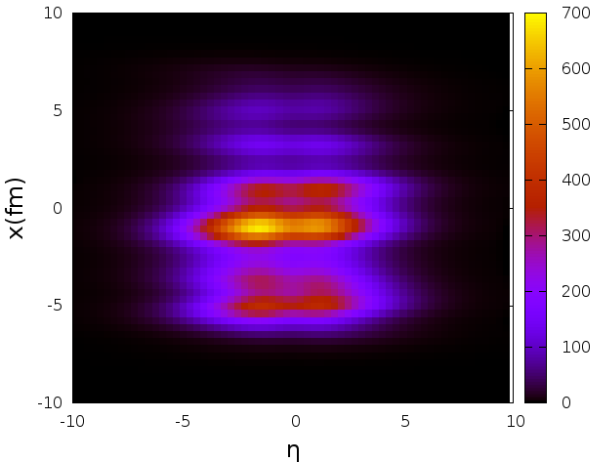

Figure 2.3: Fluctuation in the $x\eta$ plane.

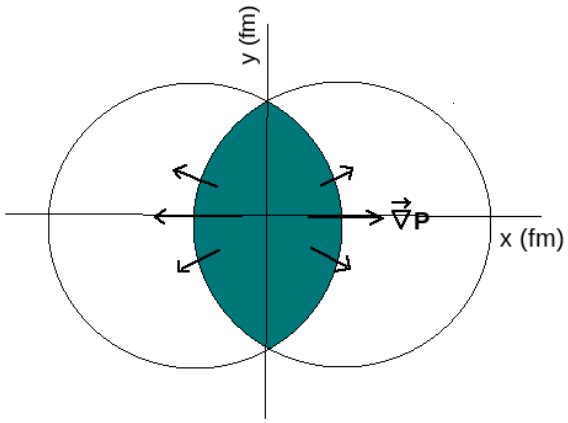

Figure 2.4: Overlapping zone of two colliding nuclei in the transverse plane. Pressure gradients are created because of the spatial asymmetry.

extension of the above discussed initial-condition model with fluctuations in the longitudinal pseudorapidity direction also [5]. We use 0-1% central Pb+Pb collision events at 5.02 TeV. Figs. (2.2) and (2.3) display initial density profile in a typical collision event.

2.1.3 Eccentricity

The overlapping zone of two nuclei has almond-shaped asymmetry as shown in Fig. (2.4). When the collision is 0% central, the eccentricity, $\varepsilon \approx 0$. As the collision becomes more and more peripheral, ε approaches 1. The variation of ε with centrality is shown in Fig. (2.5).

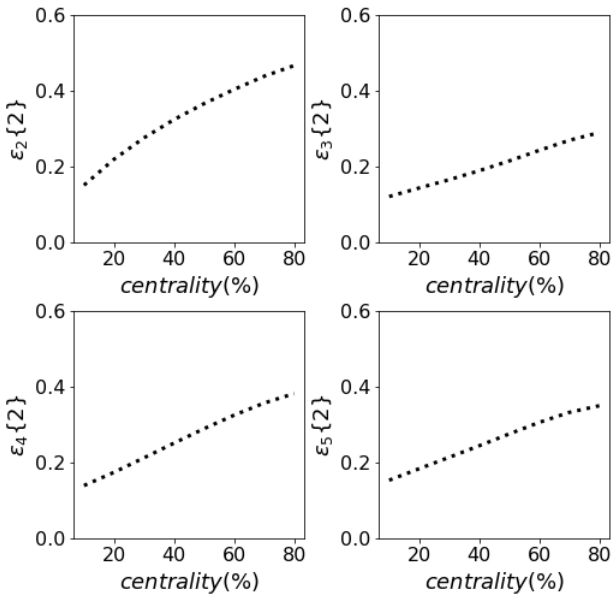

Figure 2.5: Centrality dependence of the root mean square eccentricities

. The spatial anisotropies in the initial energy density profile are characterized by the eccentricity coefficient ε_n and the associated angle Φ_n.

$$\Sigma_n \equiv \varepsilon_n e^{in\Phi_n} \equiv -\frac{\int r dr d\phi r^n e^{in\phi} e(r,\phi)}{\int r dr d\phi r^n e(r,\phi)} = -\left\langle e^{in\phi} \right\rangle, \quad n > 1 \tag{2.7}$$

where $e(r,\phi)$ is the initial energy density distribution in the transverse plane, and n is the harmonic index.

2.2 Hydrodynamic modelling

The simulation with T_RENTo provides an initial density profile with many discrete sources of energy in the (x, y, η) space. These point sources are smeared assuming a smooth Gaussian profile over each energy density point. Essentially each participant nucleon is a source of energy density now. Summing over all the participant nucleons provides us a smooth Gaussian energy source which ensures a local thermal equilibrium so that hydrodynamics

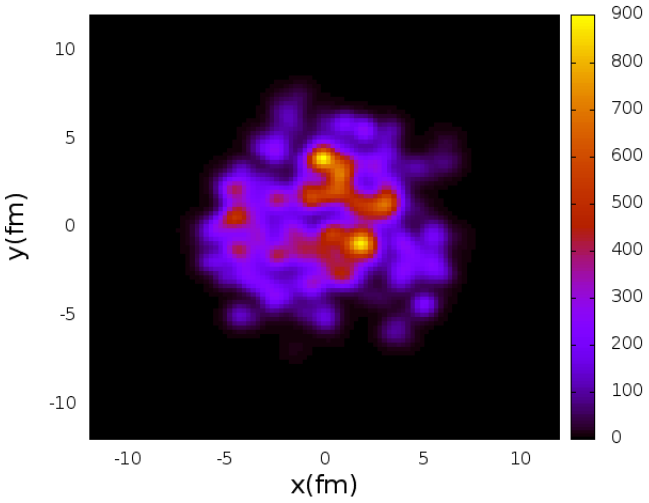

Figure 2.6: Energy density distribution at $\tau_0 = 0.2$ fm/c

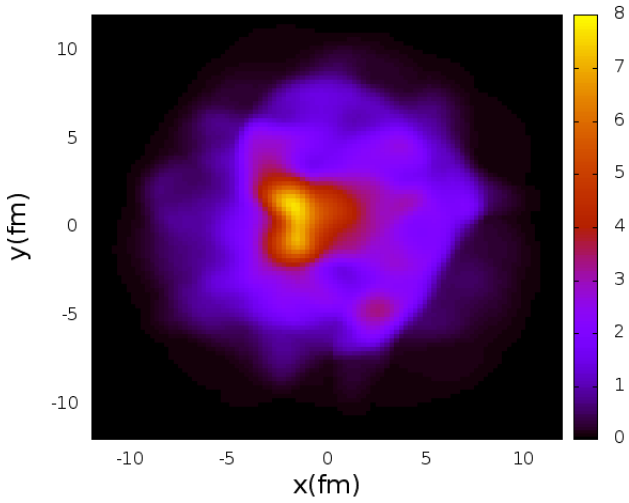

Figure 2.7: Energy density distribution at $\tau = 5$ fm/c

can take place now. The initial density profile from T_RENTo 3D is fed into a hydrodynamic model, where it undergoes hydrodynamical expansion through the equation of state and conservation laws, followed by freezing out to hadron gas. Our choice of (3+1)-dimensional viscous hydrodynamic model is $MUSIC$, Monotonic Upwind Scheme for conservation laws of Ion Collisions [6]. In $MUSIC$, Kurganov-Tadmor algorithm is used to solve hydrodynamic equations. Figs. (2.6) and (2.7) shows the time evolution of energy density and smoothening due to hydrodynamics.

2.2.1 Relativistic hydrodynamics

The degrees of freedom of a relativistic fluid component are Lorentz four-vector flow u^μ, energy density ϵ, the pressure P and the baryon energy density ρ_B. $\mu = 0, 1, 2, 3$ denotes Minkowski 4-space with metric $g^{\mu\nu} = \text{diag}(+,-,-,-)$. The six dynamic quantities such as energy density, pressure, the three components of flow vector (the fourth component is constrained by the relation, $u^\mu u_\nu = 1$) and ρ_B are linked by the conservation laws,

$$\partial_\mu T^{\mu\nu} = 0 \tag{2.8}$$

$$\partial_\mu J^\mu_B = 0 \tag{2.9}$$

and the equation of state,

$$P = P(\epsilon, \rho_B). \tag{2.10}$$

$T^{\mu\nu}$ is the energy-momentum tensor and J^{μ}_{B} is the net baryon current density. The net baryon number density is negligible in the central region for RHIC and LHC. So J^{μ}_{B} is essentially zero.

When the system is exactly at local thermal equilibrium, it is described by ideal hydrodynamics. In this case, $T^{\mu\nu}$ is defined as

$$T^{\mu\nu}{}_{\text{ideal}} = \epsilon u^{\mu} u^{\nu} - \Delta^{\mu\nu} P, \quad \text{where} \quad \Delta^{\mu\nu} = g^{\mu\nu} - u^{\mu} u^{\nu}, \tag{2.11}$$

the projector transverse to the flow velocity. System which deviates from local equilibrium can be described by viscous hydrodynamics.

$$T^{\mu\nu} = \epsilon u^{\mu} u^{\nu} - \Delta^{\mu\nu}(P + \Pi) + \pi^{\mu\nu} \tag{2.12}$$

in the case of viscous hydrodynamics. The shear viscous pressure, $\pi^{\mu\nu}$ and the bulk viscous pressure, Π contain information about the deviation of the system from local thermal equilibrium.

2.2.2 Coordinate system

The plane perpendicular to the collision axis is called the transverse plane. For each particle emitted, transverse momentum p_T and azimuthal angle φ are defined as shown in Fig. (2.8). The variables defined in the direction of the collision axis are the momentum rapidity y and pseudorapidity η. They are defined as,

$$y \equiv \frac{1}{2} \ln \frac{E + p_z}{E - p_z}, \tag{2.13}$$

$$\eta \equiv -\ln \tan \frac{\theta}{2} = \frac{1}{2} \ln \frac{|\mathbf{p}| + p_z}{|\mathbf{p}| - p_z}, \tag{2.14}$$

where E is the energy and $\mathbf{p}$ is the momentum vector of the particle emitted. p_z is the component of momentum along the collision axis and θ is the angle between the momentum vector of the particle and the collision axis. Since it is difficult to measure the two quantities

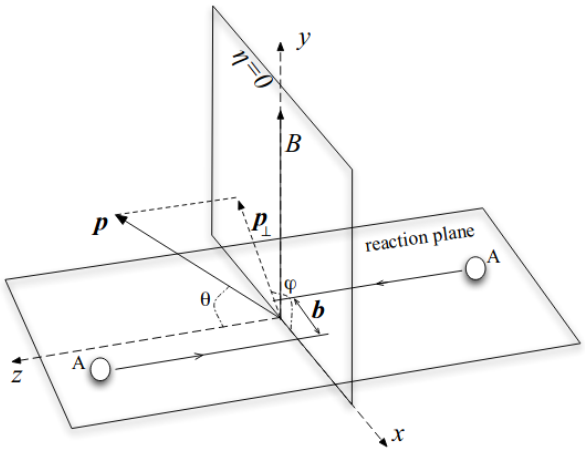

Figure 2.8: Coordinates of heavy-ion collision[7].

namely E and p_z of each particle emitted, pseudorapidity which requires only θ is preferred over momentum rapidity for experimental purposes.

In high-energy reactions, nearly uniform energy deposition is observed as a function of rapidity y, which is consistent with the boost-invariance approximation. So hyperbolic coordinates (τ, η_s) which make use of this symmetry are preferred:

$$\tau = \sqrt{t^2 - z^2}, \tag{2.15}$$

$$\tanh \eta_s = \frac{z}{t}. \tag{2.16}$$

(In the boost-invariance approximation, $y = \eta_s$.) Since in this thesis, we are focusing on fluctuations in the longitudinal direction, we cannot use the boost-invariance approximation. Fully fluctuating (3+1)D initial density model with hydrodynamic expansion in three dimensions is used in our work.

2.2.3 Transport coefficients

Shear viscosity coefficient and bulk viscosity coefficient are the two important transport coefficients which characterize the dynamic properties of a fluid. Resistance of the fluid to shear strain is characterized by the dimensionless quantity, ratio of shear viscosity coefficient to entropy density, η/s. The strongly interacting QGP has a small viscosity. String theory

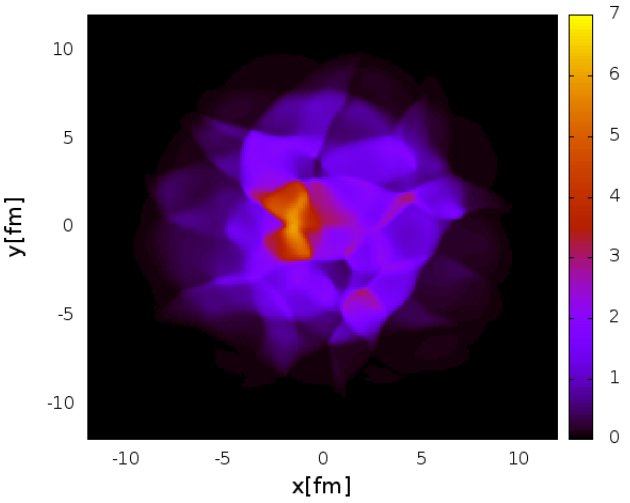

Figure 2.9: Energy density distribution at $\tau = 5$ fm/c, $\eta/s = 0$

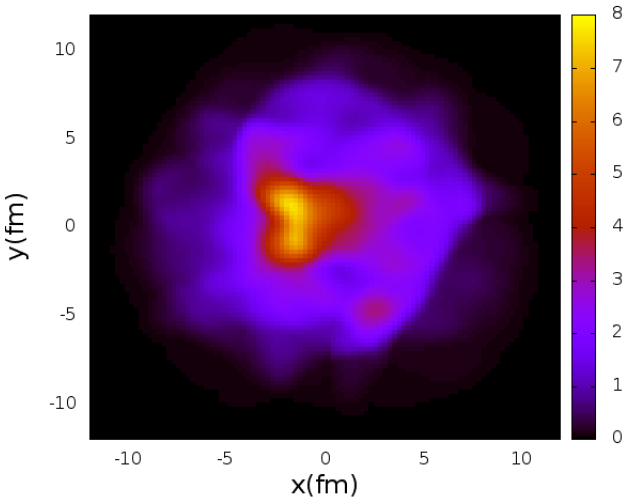

Figure 2.10: Energy density distribution at $\tau = 5$ fm/c, $\eta/s = 0.12$

provides a lower limit for the specific shear viscosity η/s as $1/4\pi \approx 0.08$. Presence of viscosity in the fluid smoothens out the small-scale lumps in the energy density distribution as it evolves and makes it more isotropic. This is shown in Figs. (2.9) and (2.10).

Bulk viscosity describes the fluid resistance to volume strain. But it does not make any qualitative difference in the hydrodynamic expansion rate. For our purposes, we are using an $\eta/s = 0.08$ without turning on the bulk viscosity effect.

2.2.4 Equation of state

Equation of state (EOS) connects the local thermodynamic quantities: pressure, P and energy density, ϵ. The relation $P = P(\epsilon)$ is required to close the conservation laws. The EOS is modelled from lattice-based quantum chromodynamics (QCD) calculations. It has been observed that lattice QCD calculations agree remarkably well with the thermodynamic properties of hadron resonance gas (HRG) at low temperatures. This is shown in Fig. (2.11). After the hydrodynamical expansion, the system reaches a state where hadrons are formed. Hydrodynamic description based only on quarks and gluons is not valid now, and an EOS which incorporates the dynamics of hadrons is needed. In our work we are using a lattice based EOS parametrization "s95p-PCE-v1" [8]. Here, HRG at low temperatures is extrapolated to lattice results at higher temperatures. This model

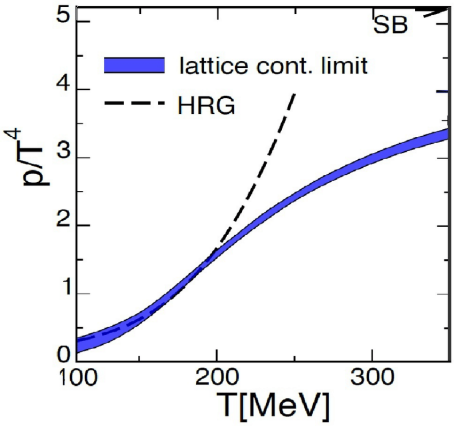

Figure 2.11: Below 200 MeV, lattice QCD calculations matches with HRG [9].

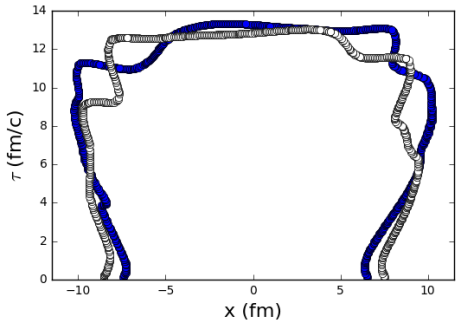

Figure 2.12: Freeze-out surfaces of two different events.

implements a partial chemical equilibrium at $T = 150$ MeV. Below the chemical freeze-out temperature, $T_{chem} = 150$ MeV, the total densities (including the densities from resonance decay of unstable species) of stable hadrons are conserved. As explained in section 1.2, hadrons will undergo kinetic freeze-out after the chemical freeze-out where even elastic scatterings between the hadrons stop. Figure. (2.12) shows the kinetic freeze-out surfaces in the x-τ plane for two different events.

2.3 Particlization dynamics

Some heavy-ion collision models are designed by combining a hydrodynamical model to describe the evolution when the system is partonic and a hadronic transport model like UrQMD to describe the evolution post hadronization. The surface on which the transition from fluid to cascade is chosen to be the surface of constant temperature, T_{sw} [10]. The reason for this choice is that the mean-free path is an important quantity for a system in local thermal equilibrium and temperature is a monotonous function of mean-free path (the higher the temperature of the liquid, the lower is the mean-free path). The switch does not happen at kinetic freeze-out. Because after kinetic freeze-out, the only process remaining is resonance decay. Transport model is not required for that. The switch does not happen at hadronization either. The reason is that the confinement of partons into hadrons is a smooth crossover transition. So we choose the switching surface to be at a temperature where hadronization has already occurred and close to the crossover transition temperature

as shown in Fig. (1.2), where the physics of the system does not change.

The information from the freeze-out is used to calculate the distribution of particles with well-defined positions and momenta, and this is done by a procedure proposed by Cooper and Frye. This distribution is then used as the initial state of the hadron transport model, which describes the properties of the system until kinetic freeze-out.

The freeze-out hypersurface in the four-dimensional (τ, x, y, η) space has information about the system at all $T > T_{sw}$, when it was undergoing hydrodynamical expansion. The particle distribution is calculated using the Cooper-Frye formula [11],

$$E\frac{dN}{d^3p} = \frac{dN}{dy p_T dp_T d\phi_p} = g_i \int_\Sigma f(u^\mu p_\mu) p^\mu d\Sigma_\mu, \tag{2.17}$$

with the distribution function,

$$f_{B/F}(u^\mu p_\mu) = \frac{1}{(2\pi)^3} \frac{1}{\exp(u^\mu p_\mu / T) \pm 1} \tag{2.18}$$

In computational model, the integral is replaced by summation and the $d^3\Sigma_\mu$ by $\Delta^3\Sigma_\mu$. In Eq. (2.17), g_i is the degeneracy of particle species i. The integral runs over the surface Σ, $d\Sigma_0 = d^3r$ and $d\mathbf{\Sigma} = d\tau d^2s\mathbf{n}$ is the hypersurface element in the four-dimensional space (τ, x, y, η). $\mathbf{n}$ is the unit vector normal to the hypersurface. When the system is exactly in thermal equilibrium, it can be described by Bose-Einstein or Fermi-Dirac distribution function as shown in Eq. (2.18). The upper sign corresponds to fermions and lower to bosons. But when studying a system with viscous effects, correction functions are added to the distribution function.
According to the kinetic theory, for a non-interacting gas,

$$T^{\mu\nu} = \sum_{species} g \int \frac{d^3p}{(2\pi)^3} \frac{p^\mu p^\nu}{E} f(p). \tag{2.19}$$

According to viscous hydrodynamics,

$$T^{\mu\nu} = \epsilon u^\mu u^\nu - \Delta^{\mu\nu}(P + \Pi) + \pi^{\mu\nu} \tag{2.20}$$

In order to match Eq. (2.19) and Eq. (2.20), that is, to consider the viscous effects in the kinetic theory, the only way is to modify the distribution function by adding viscous

corrections

$$f_{B/F} = f^{(0)}_{B/F} + \delta f^{shear}_{B/F} + \delta f^{bulk}_{B/F} \tag{2.21}$$

where $f^{(0)}_{B/F}$ is the thermal Bose-Einstein or Fermi-Dirac distribution function, $\delta f^{shear}_{B/F}$ is the viscous correction due to shear stress tensor $\pi^{\mu\mu}$ and $\delta f^{bulk}_{B/F}$ is the viscous correction due to bulk pressure Π.

2.4 Post-particlization dynamics

After particlization, the system consists of hadron gas with particles undergoing inelastic and elastic collisions with each other until the final freeze-out. Unstable hadron species decay into stable hadron species. Due to inelastic collisions and decays, the relative abundance of each hadron species changes, and due to elastic collisions, the momentum distribution function gets modified. This entire post-particlization dynamics is modelled using kinetic theory.

The viscous hydrodynamic code MUSIC incorporates the transport model called UrQMD (Ultra-relativistic Quantum Molecular Dynamics) for describing the post-particlization dynamics. UrQMD solves the coupled Boltzmann equations, $df_i(x,p)/dt = C_i(x,p)$, where f_i is the distribution function of species i and C_i is the term which has information about collisions of i^{th} species with others. After the final freeze-out, hadronic observables are calculated from the momentum spectra of each particle.

Chapter 3

Hadronic observables

The most significant and convincing evidence for hydrodynamical description of heavy-ion collisions is the anisotropic distribution of charged hadrons. One can investigate the signature of the initial state in the final distribution of particles by studying the flow anisotropies. When two Lorentz-contracted nuclei collide along the longitudinal axis, significant amount of their kinetic energy is deposited in the mid-rapidity region. The distance between the centers of the two nuclei is defined as the impact parameter, b. Experimentally, one has no control over the value of b. It is highly unlikely for the overlapping region of two nuclei to have an azimuthal symmetry in the transverse plane. Indeed it acquires an approximate elliptical shape. Due to the geometrical reasons, anisotropic pressure gradients are developed which drive the hydrodynamical expansion. When hadrons are finally formed, this initial spatial anisotropy gets imprinted on the hadrons as momentum anisotropy. In the direction where the fluid is compressed more, larger pressure gradients are developed and more energetic particles are emitted, e.g., at $\phi \approx 0$ and $\phi \approx \pi$) as depicted in Fig. (3.1). It is understood that the azimuthal anisotropies in the distribution of final-state particles is the hydrodynamic response to the anisotropies in the initial state [12].

3.1 Quantifying momentum anisotropy

The hydrodynamic response to the spatial anisotropy in the initial density profile is captured by the anisotropic flow coefficient v_n and the associated event plane angle Ψ_n. The flow vector

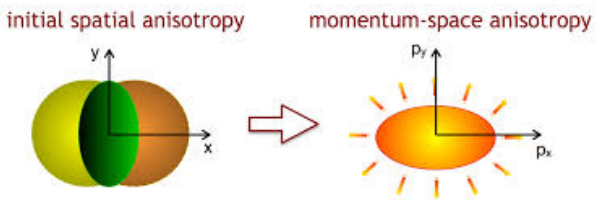

Figure 3.1: Conversion of spatial anisotropy into momentum anisotropy

V_n is defined as,

$$V_n = v_n e^{in\Psi_n} \equiv \langle e^{in\varphi} \rangle \tag{3.1}$$

where φ is the azimuthal angle of transverse momentum of the emitted particle, and the average runs over particles in an event and then over events in a centrality class.

From Eq. (3.1), we can write that

$$v_n = \langle \cos[n(\varphi - \Psi_n)] \rangle, \tag{3.2}$$

since averaging over many events results in a vanishing imaginary part of the flow vector.

The momentum anisotropies of emitted particles are typically quantified as Fourier coefficients of azimuthal distribution of particles [13]. Consider a periodic function, $f(x)$ with period 2π. On Fourier expansion,

$$f(x) = \frac{a_0}{2} + \sum_{n=1}^{\infty} a_n \cos(nx) + \sum_{n=1}^{\infty} b_n \sin(nx) \tag{3.3}$$

If we impose the constraints, $\int_0^{2\pi} f(x)dx = 1$ and $f(x) = f(-x)$ on Eq. (3.3) we get $a_0 = 1/\pi$ and $b_n = 0 \ \forall \ n$.

$$\langle \cos(nx) \rangle = \int_0^{2\pi} \cos(nx) f(x) dx = \sum_{m=1}^{\infty} a_m \int_0^{2\phi} \cos(nx) \cos(mx) dx = \pi a_n, \tag{3.4}$$

Now, if we consider the variable x as $(\varphi - \Psi_n)$,

$$\langle \cos[n(\varphi - \Psi_n)] \rangle = \pi a_n \tag{3.5}$$

and

$$\langle \sin[n(\varphi - \Psi)] \rangle = 0. \tag{3.6}$$

Hence,

$$f(\varphi) = \frac{1}{2\pi}\left[1 + \sum_{n=1}^{\infty} 2\langle \cos[n(\varphi - \Psi_n)] \rangle \cos[n(\varphi - \Psi_n)]\right] \tag{3.7}$$

Considering Eq. (3.2) and Eq. (3.5), $v_n = \pi a_n$. Thus v_n is the Fourier coefficient except for a factor of π.

Equation. (3.7) becomes

$$f(\varphi) = \frac{1}{2\pi}\left[1 + \sum_{n=1}^{\infty} 2v_n \cos[n(\varphi - \Psi_n)]\right] \tag{3.8}$$

And, one can assume that, at the end of the evolution, particles are emitted based on a probability distribution [14]. The azimuthal distribution of particles can be written as,

$$\frac{dN}{d\varphi} \propto 1 + \sum_{n=1}^{\infty} 2v_n \cos[n(\varphi - \Psi_n)] = \sum_{n=-\infty}^{\infty} v_n e^{in\Psi_n} e^{-in\varphi} = \sum_{n=-\infty}^{\infty} V_n e^{-in\varphi}, \tag{3.9}$$

where n is the harmonic index which is the order of anisotropy. v_1, v_2 and v_3 are called directed, elliptic and triangular flows, respectively. These names are based on the shapes of polar plots shown in Fig. (3.2). The geometry of the overlapping region contributes to the even harmonics, n = 2,4,6, ... and it cannot contribute to odd harmonics. Until recently, it was assumed that because of the symmetry of the colliding identical nuclei, $\Psi_n \approx 0$ for n = odd. But RHIC and LHC have observed odd harmonics which explain the fluctuations in the geometry of the overlapping area.

The set of complex Fourier coefficients V_n represents the anisotropic flow which fluctuates from event to event. Both v_n and Ψ_n in principle depend on transverse momentum p_T and pseudorapidity η. It has the following properties. $V_n(p) = V^*_{-n}(p)$ and $V_0(p)$ is real. The variable p stands for (p_T, η). The usual definition of flow coefficient is $v_n = |V_n|/V_0$ which is real and normalized.

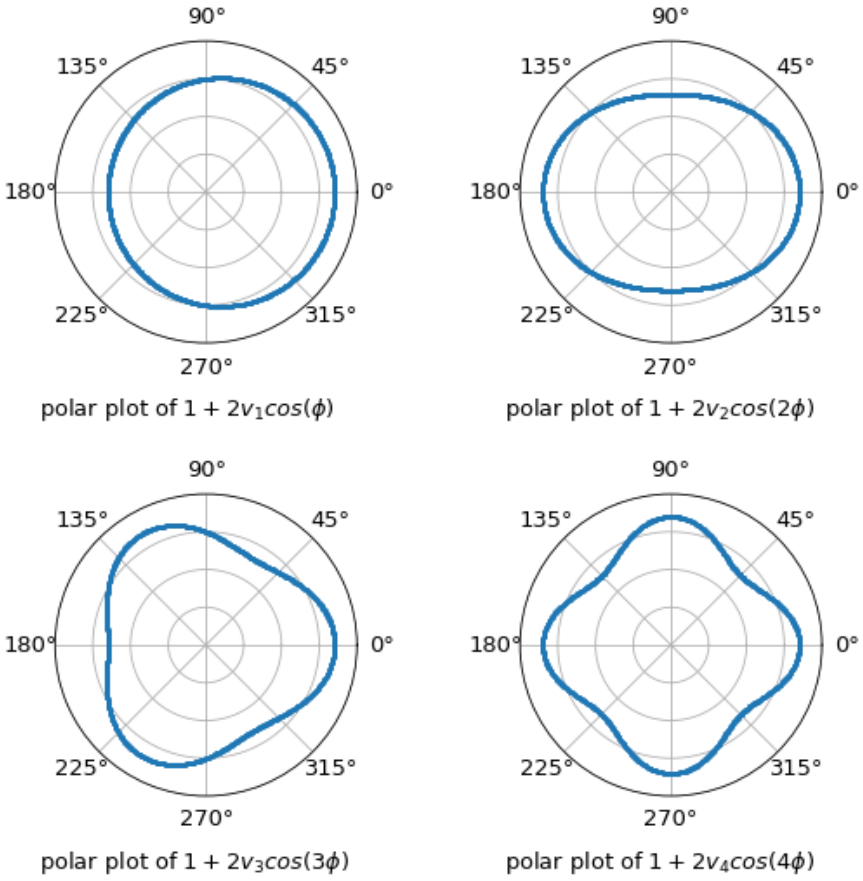

Figure 3.2: Polar plots of flow coefficients

In general, the flow vector is written as

$$v_n e^{in\Psi_n}(p_T, \eta) \equiv \frac{\int d\varphi e^{in\varphi} \frac{dN_{ch}}{d\eta dp_T d\varphi}}{\int d\varphi \frac{dN_{ch}}{d\eta dp_T d\varphi}} \tag{3.10}$$

In this thesis, we are interested in the p_T-integrated flow coefficient at each η. We modify the hydrodynamic code MUSIC such that the flow coefficient is defined in the following way for each event.

$$v_n e^{in\Psi_n}(\eta) \equiv \frac{\int d\varphi dp_T e^{in\varphi} \frac{dN_{ch}}{d\eta dp_T d\varphi}}{\int d\varphi dp_T \frac{dN_{ch}}{d\eta dp_T d\varphi}} \tag{3.11}$$

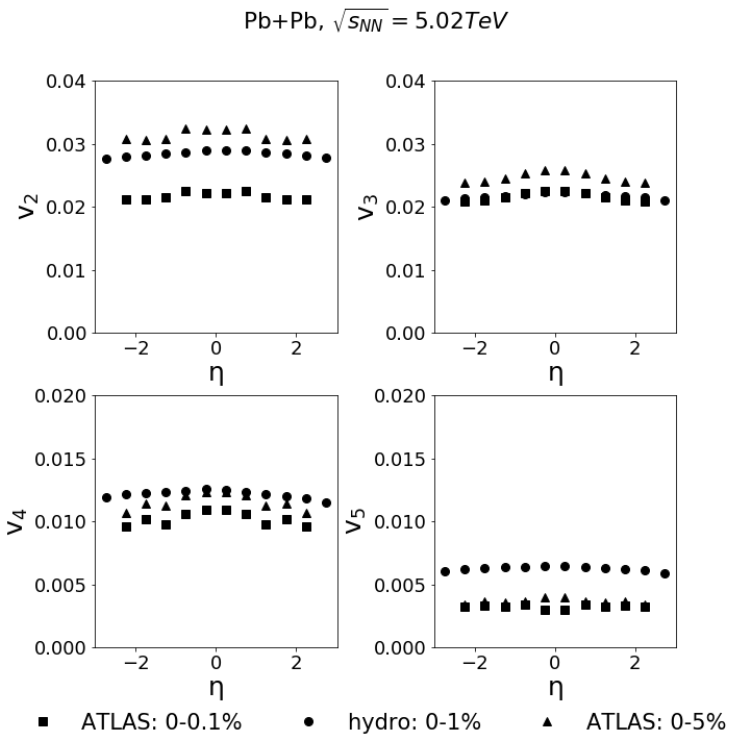

Figure 3.3: η dependence of v_n

The variation of flow coefficient with pseudorapidity is shown in Fig. (3.3). The hydrodynamical evolution with MUSIC is simulated with Pb+Pb collision at $\sqrt{s_{NN}}$ =5.02 TeV with p_T ranging from 0.2 GeV to 3 GeV and η ranging from -3 to +3 with 12 bins for the 0-1% central Pb+Pb collision events generated by T_RENTo 3D. The pseudorapidity dependence of the flow coefficient v_n has not yet been measured experimentally for 0-1% central Pb+Pb collision at $\sqrt{s_{NN}}$ =5.02 TeV. Flow coefficients from hydrodynamical simulation in 0-1% centrality bin are compared with flow coefficients from ATLAS data in 0-0.1% and 0-5% centrality bins [15]. As explained earlier, when the collision is more peripheral, anisotropy in the distribution of particles, quantified by the flow coefficient v_n, increases. This trend is clearly visible in Fig. (3.3). v_n for 0-0.1% is smaller and v_n for 0-5% is larger while v_n for 0-1% sits in between the curves.

The trend is not very clear in the case of higher harmonics. This can be due to the difference in the definitions of flow coefficients experimentally and theoretically. The multiple definitions are due to the reason that v_n of a single event is impossible to measure directly in experiments. Although different definitions are used, they only differ by 10-20%.

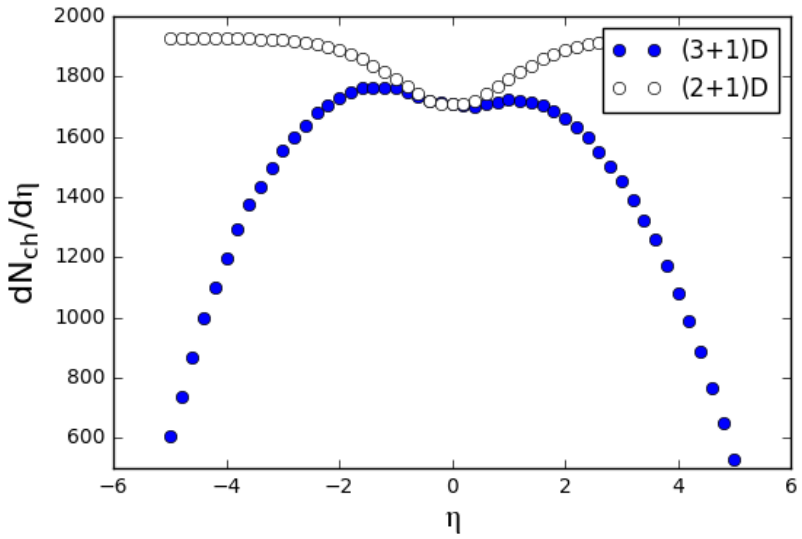

Figure 3.4: Pseudorapidity distribution of charged particles

Experimentally, in "scalar-product method" v_n is measured as,

$$v_n^{exp} = \sqrt{\left\langle \langle e^{in(\varphi_1 - \varphi_2)} \rangle_{particles} \right\rangle_{events}}, \tag{3.12}$$

where the inner bracket represent average over all charged hadrons within an event and the outer bracket represents average over all events in a centrality bin. v_n is calculated theoretically as follows.

$$v_n^{th} = \sqrt{\langle v_n^2 \rangle_{events}}, \tag{3.13}$$

where v_n inside the brackets is for one event which is obtained from hydrodynamic simulation model and the brackets represent average over all events in a centrality bin.

3.2 Charged hadron multiplicity

Another interesting hadronic observable is the charged hadron multiplicity. The distribution of charged hadron multiplicity as a function of pseudorapidity is shown in Fig. (3.4). Boost invariance had been observed in RHIC and LHC in a small region in mid-rapidity. Open circles represent 2+1 D calculations which assumes complete boost invariance.

3.3 Flow correlation

According to the definition of v_n in Eq. (3.1), measuring them is experimentally difficult because event plane orientation Ψ_n is not directly measurable. In order to overcome this drawback, the method of multi-particle azimuthal correlation has been employed to measure the flow coefficients. In the two-particle correlation method, instead of measuring Ψ_n, one fixes the difference between azimuthal angles of two particles $\Delta\varphi = \varphi^{(1)} - \varphi^{(2)}$ and then measures the number of charged particle-pairs with that $\Delta\varphi$. Since the azimuthal orientation of every collision is not controlled, the quantities which are invariant under rotation are measured. The method of multi-particle particle correlation is well suitable in that aspect also.

Two-particle correlation measured by CMS experiment is shown in Fig. (3.5). The number of particle pairs at each $(\Delta\varphi, \Delta\eta)$, is shown as a three-dimensional histogram as a function of $\Delta\varphi$ and $\Delta\eta$. The important feature in the figure is gradual change which is actually a signature of fluid behaviour. The extension of "ridge" in the pseudorapidity direction indicates the collective behavior. A long-range ridge with maximum values of particle-pairs observed is visible at $\Delta\varphi = \pi$. This describes the elliptic flow. The peak visible at $\Delta\varphi \approx \Delta\eta \approx 0$ describes the jets that come from short-range correlations.

At the end of the collective expansion particles are emitted based on the probability distribution, Eq. (3.9) which depends on the initial geometry as well. In general particles are not emitted independently[17]. So the distribution of particle-pairs can be written as,

$$\frac{dN_{pairs}}{d\mathbf{p}_1 d\mathbf{p}_2} = \frac{dN}{d\mathbf{p}_1}\frac{dN}{d\mathbf{p}_2} + \delta(\mathbf{p}_1, \mathbf{p}_2). \tag{3.14}$$

The term $\delta(\mathbf{p}_1, \mathbf{p}_2)$ corresponds to the intrinsic particle correlations that come neither from initial geometry nor from the hydrodynamic expansion. They denote correlations from resonance decay, jets, final state particle interactions etc. They are called direct or non-flow correlations. Since these correlations do not contain any information about the geometry of the reaction plane, we are not interested in them.

The collective behaviour of the expansion is entirely coming from the first term of Eq. (3.14) which only depends on the single particle distribution function. When non-flow

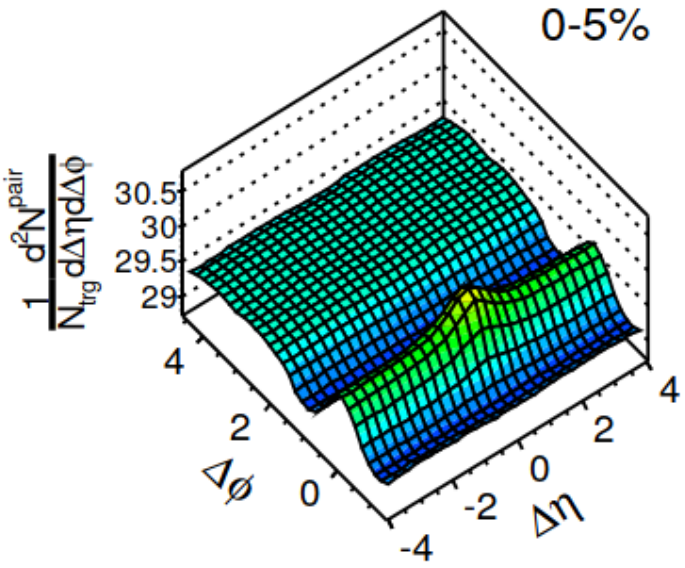

Figure 3.5: Two particle correlation function for Pb+Pb collision at 5.02 TeV for 0-5% central events [16].

terms are not there, the pair distribution is simply the product of single particle distributions, showing that particles are emitted independently. This is the signature of collective flow. These terms are called indirect or flow correlations.

The event to event fluctuations impart a statistical uncertainty of approximately $1/\sqrt{N_{ev}}$ in the values of flow coefficients, where N_{ev} is the number of events. Therefore, one needs to simulate enough number of events and deal with averaged quantities.

The distribution of particle pairs is calculated from a sample of events and averaged.

$$\left\langle \frac{dN_{pairs}}{d\mathbf{p}_1 d\mathbf{p}_2} \right\rangle = \left\langle \frac{dN}{d\mathbf{p}_1}\frac{dN}{d\mathbf{p}_2} \right\rangle + \mathcal{O}(\mathcal{N}). \tag{3.15}$$

The non-flow terms are of order $\mathcal{N}$, while the flow terms are of order $\mathcal{N}^2$, where $\mathcal{N}$ is the approximate number of particles emitted out of each collision. So for large system, we can ignore non-flow terms although it is quite impossible to eliminate all the non-flow effects in

experiments. For our convenience, we are defining the single-particle distribution as [18],

$$\frac{dN}{d\mathbf{p}} = \sum_{n=-\infty}^{\infty} V_n(p) e^{-in\varphi}, \tag{3.16}$$

where $d\mathbf{p} \equiv dp_T d\eta d\varphi$.

$$\frac{dN}{d\mathbf{p}_1} = \sum_{n=-\infty}^{\infty} V_n(p_1) e^{-in\varphi_1} \tag{3.17}$$

and

$$\frac{dN}{d\mathbf{p}_2} = \sum_{m=-\infty}^{\infty} V_m(p_2) e^{-im\varphi_2} \tag{3.18}$$

LHS of both the equations are real. So RHS also have to be real. Taking transpose conjugate of Eq. (3.18) gives,

$$\frac{dN}{d\mathbf{p}_2} = \sum_{m=-\infty}^{\infty} V_m^*(p_2) e^{im\varphi_2}. \tag{3.19}$$

Multiplying Eq. (3.17) and Eq. (3.19) gives,

$$\frac{dN}{d\mathbf{p}_1}\frac{dN}{d\mathbf{p}_2} = \sum_{n,m=-\infty}^{\infty} V_n(p_1) V_m^*(p_2) e^{-in\varphi_1} e^{im\varphi_2}. \tag{3.20}$$

LHS of the above equation is real because it is simply the product of number of particles. In order to make the RHS also real, m has to be equal to n. So Eq. (3.20) becomes,

$$\frac{dN}{d\mathbf{p}_1}\frac{dN}{d\mathbf{p}_2} = \sum_{n=-\infty}^{\infty} V_n(p_1) V_n^*(p_2) e^{in(\varphi_2-\varphi_1)}. \tag{3.21}$$

Averaging over statistically significant number of events within a centrality bin gives,

$$\left\langle \frac{dN}{d\mathbf{p}_1}\frac{dN}{d\mathbf{p}_2} \right\rangle = \sum_{n=-\infty}^{\infty} V_{n\Delta}(p_1, p_2) e^{in(\varphi_2-\varphi_1)}, \tag{3.22}$$

where $V_{n\Delta}$ is defined as,

$$V_{n\Delta}(p_1, p_2) = \langle V_n(p_1) V_n^*(p_2) \rangle \tag{3.23}$$

The pair particle distribution is invariant under rotation which is ensured by the difference in azimuthal angles in the right hand side of the Eq. (3.22).

Since we are interested in the longitudinal fluctuations, the focus is only on p_T-integrated quantities. Our aim is to understand flow fluctuations in heavy-ion collisions by analyzing the quantity $V_{n\Delta}(p_1, p_2)$ through a statistical procedure called principal component analysis which is described in the upcoming chapters.

Chapter 4

Modes of fluctuations

The different modes of flow fluctuations give additional information on the initial state of heavy-ion collisions. Our aim is to apply the method of principle component analysis (PCA) to study the event-by-event fluctuations of the anisotropic flow in the longitudinal direction. In this chapter, the leading and sub-leading components of anisotropic flow are explored.

4.1 Principal component analysis

Principal component analysis is a powerful statistical technique which basically reduces the dimensions of the data set [19]. Using this technique, an original set of correlated variables can be linearly transformed into an uncorrelated smaller set of variables called principal components. The beauty is that the final smaller set of data contains all the essential information in the original set of data. Thus all the information contained in two-particle correlation can be studied by applying PCA to multiplicity fluctuations and flow coefficients fluctuations.

4.1.1 Geometric representation of principal components

An illustration of PCA is shown below. Imagine x_1 and x_2 denote two properties of a $n-$sized sample. Our interest is the correlation between these two variable. Figure. (4.1) shows 2D

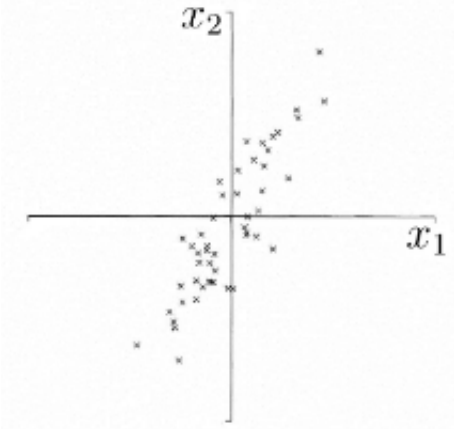

Figure 4.1: A plot of n observations on variables x_1, x_2

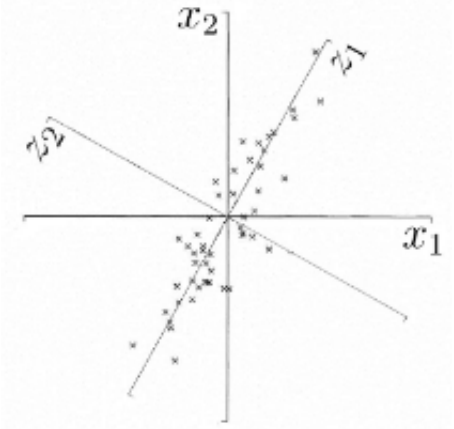

Figure 4.2: First component z_1 and second component z_2

representation of two variables $\mathbf{x} = (x_1, x_2)$.

It is clear from the figure that the two variables are correlated. So a new variable can be constructed out of the two variables x_1 and x_2, which is a new property of the $n-$sized sample. The new variable is constructed as a linear combination of the two variables, $z_1 = ax_1 + bx_2$ where a and b correspond to the best fit of the line to the n-sized data. It is plotted in Fig. (4.2).

The method of PCA finds the best fit line z_1 by imposing two constraints: minimizing the error of each point on the fit line and maximizing the spread of projection of points on the line. By pythagoras theorem, the higher variance implies lower error. z_1 is called the first principal component. z_2 is the best fit to the sample in the plane perpendicular to the first principal component. Principal components are linear least fits to a sample, each fit orthogonal to all the previous fits.

4.1.2 Derivation of principal components

Suppose $\mathbf{x}$ is a vector and each component of the vector is an observation: $\mathbf{x} = (x_1, x_2, x_3, ..., x_p)$. We construct a vector $\alpha_1 = \alpha_{11}, \alpha_{12}, \alpha_{13}, ..., \alpha_{1p}$. The first principal

component is gives as,

$$\alpha_{\mathbf{1}}^{\mathbf{T}}\mathbf{x} = \alpha_{11}x_1 + \alpha_{12}x_2 + \alpha_{13}x_3 + ... + \alpha_{1p}x_p = \sum_{j=1}^{p} \alpha_{1j}x_j, \tag{4.1}$$

subject to the constraint var$[\alpha_1^T x]$ is maximum. Similarly, k^{th} PC is defined as,

$$\alpha_{\mathbf{k}}^{\mathbf{T}}\mathbf{x} = \alpha_{k1}x_1 + \alpha_{k2}x_2 + \alpha_{k3}x_3 + ... + \alpha_{kp}x_p = \sum_{j=1}^{p} \alpha_{kj}x_j, \tag{4.2}$$

subject to the constraints, var$[\alpha_{\mathbf{k}}^{\mathbf{T}}\mathbf{x}]$ is maximum, cov$[\alpha_{\mathbf{k}}^{\mathbf{T}}\mathbf{x},\alpha_{\mathbf{l}}^{\mathbf{T}}\mathbf{x}] = 0$ and $\alpha_{\mathbf{k}}^{\mathbf{T}}\alpha_{\mathbf{k}} = 1$.

Suppose $\mathbf{S}$ represents the covariance matrix of the vector $\mathbf{x}$, where the term $(i, j)^{th}$ element is the covariance between i^{th} and j^{th} element of $\mathbf{x}$ when $i \neq j$ and variance when $i = j$. One need to maximize var$[\alpha_{\mathbf{k}}^{\mathbf{T}}\mathbf{x}] = \alpha_{\mathbf{k}}^{\mathbf{T}}\mathbf{S}\alpha_{\mathbf{k}}$ with the constraint $\alpha_{\mathbf{k}}^{\mathbf{T}}\alpha_{\mathbf{k}} = 1$. This is done through the approach of Lagrange multipliers.

The idea is to maximize,

$$\alpha_{\mathbf{k}}^{\mathbf{T}}\mathbf{S}\alpha_{\mathbf{k}} - \lambda_k(\alpha_{\mathbf{k}}^{\mathbf{T}}\alpha_{\mathbf{k}} - 1), \tag{4.3}$$

where λ is the lagrange multiplier. In order to find the maximum of the above quantity, we set the first derivative to zero. Differentiating with respect to α_k gives,

$$\mathbf{S}\alpha_{\mathbf{k}} = \lambda_k\alpha_{\mathbf{k}} \tag{4.4}$$

The above equation indicates λ is the eigenvalue of the covariance matrix $\mathbf{S}$ and α_k is the corresponding eigenvector. The quantity which is to be maximized is,

$$\alpha_{\mathbf{k}}^{\mathbf{T}}\mathbf{S}\alpha_{\mathbf{k}} = \alpha_{\mathbf{k}}^{\mathbf{T}}\lambda_{\mathbf{k}}\alpha_{\mathbf{k}} = \lambda_k\alpha_{\mathbf{k}}^{\mathbf{T}}\alpha_{\mathbf{k}} = \lambda_k. \tag{4.5}$$

The k^{th} PC is $\alpha_{\mathbf{k}}^{\mathbf{T}}\mathbf{x}$ and kth largest eigenvalue is λ_k. Another constraint between eigenvalues is that, cov$[\alpha_{\mathbf{k}}^{\mathbf{T}}\mathbf{x},\alpha_{\mathbf{l}}^{\mathbf{T}}\mathbf{x}] = 0$ for $k \neq l$.

$$cov[\alpha_{\mathbf{k}}^{\mathbf{T}}\mathbf{x}, \alpha_{\mathbf{l}}^{\mathbf{T}}\mathbf{x}] = \alpha_{\mathbf{k}}^{\mathbf{T}}\mathbf{S}\alpha_{\mathbf{l}} = \lambda_l\alpha_{\mathbf{k}}^{\mathbf{T}}\alpha_{\mathbf{l}}. \tag{4.6}$$

The eigenvectors $\alpha_{\mathbf{k}}$ and $\alpha_{\mathbf{l}}$ should obey the constraint that $\alpha_{\mathbf{k}}^{\mathbf{T}}\alpha_{\mathbf{l}} = 0$ for $\alpha_{\mathbf{k}}^{\mathbf{T}}\mathbf{x}$ and $\alpha_{\mathbf{l}}^{\mathbf{T}}\mathbf{x}$ to be PCs.

As a conclusion, the k^{th} largest eigenvalue of $\mathbf{S}$ is the variance of the k^{th} principal component. And the k^{th} PC corresponds to the k^{th} largest variation of the sample. The covariance matrix needed for the PCA analysis from flow vectors is discussed in the next section.

4.2 Analyzing strategy

In this section, we discuss the construction of the correlation matrix $V_{n\Delta}(p_1, p_2)$ introduced in the previous chapter and the analysis procedure using PCA. We show how PCA reveals information about pseudorapidity dependence of flow fluctuations. The leading and sub-leading modes of multiplicity and flow fluctuation are obtained and discussed in detail.

4.2.1 Construction of correlation matrix

We construct a matrix using the Eq. (3.23) where the variable $p = \eta$ varies from -3 to 3. We divide the detector acceptance into $N_b = 12$ bins in η. Now the matrix is a 12×12 matrix where each element $V_{n\Delta}(\eta_1, \eta_2)$ measures the correlation between flow at bins η_1 and η_2. The correlation matrix is a covariance matrix by construction. Therefore, it is positive semidefinite. Covariance matrix has non-negative eigenvalues. Thus it is a non-trivial property of the correlation matrix to have non-negative eigenvalues. The presence of negative eigenvalues or negative diagonal elements can happen from the presence of non-flow effects such as resonance decay or jets.

For our purposes, flow vector $V_n(\eta)$ is defined as Q-vector [20],

$$Q_n(\eta) \equiv \frac{1}{2\pi\Delta p_T \Delta\eta} \sum_{j=1}^{M(\eta)} e^{in\varphi_j}, \tag{4.7}$$

where φ_j is the azimuthal angle of particle j and $M(\eta)$ is the number of particles in the corresponding η bin. The pair correlation is constructed from the Q-vectors as

$$V_{n\Delta}(\eta_1, \eta_2) \equiv \langle Q_n(\eta_1) Q_n^*(\eta_2) \rangle - \frac{\langle M(\eta_1) \rangle \delta_{\eta_1,\eta_2}}{(2\pi\Delta p_T \Delta\eta)^2} - \langle Q_n(\eta_1) \rangle \langle Q_n^*(\eta_2) \rangle \tag{4.8}$$

The above equation with RHS without the second term is a covariance matrix and has positive eigenvalues. The second term on RHS denotes self-correlations. After subtracting self-correlations, we might not get positive eigenvalues since by construction the matrix is not covariance matrix. But if the non-flow effects are not very significant, it should not affect the covariance matrix. Because self-correlations are basically interactions between particles coming from the same pseudorapidity bins which account for the non-flow effects. So if correlations are due to flow, eigenvalues are expected to be positive.

In our definition of Q-vector, we are not following the usual definition as in Eq. (3.1) where the flow vector is normalized with the number of particles. Instead, we are summing over the pairs because it gives weight to a bin on the order of number of particles it contains.

4.2.2 PCA on correlation matrix

Since $V_{n\Delta}(\eta_1, \eta_2)$ is a covariance matrix, principal component analysis can be performed to get the eigenvalues and eigenvectors [18].

$$V_{n\Delta}(\eta_1, \eta_2) \approx \sum_{\alpha=1}^{k} \lambda_n^{(\alpha)} \psi_n^{(\alpha)}(\eta_1) \psi_n^{(\alpha)*}(\eta_2), \tag{4.9}$$

where $\lambda_n^{(\alpha)}$ and $\psi_n^{(\alpha)}$ are the corresponding eigenvalues and normalized eigenvectors of the correlation matrix $V_{n\Delta}(\eta_1, \eta_2)$ and $k \leq N_b$.

The 12×12 matrix $V_{n\Delta}$ is diagonalized to obtain a maximum of 12 eigenvalues and corresponding 12 eigenvectors. But PCA finds out the principal modes which causes most of the variation in the fluctuating flow vectors. Thus it arranges the significant eigenvalues $\lambda_n^{(\alpha)}$ in the order of decreasing, $\lambda_n^{(1)} > \lambda_n^{(2)} > \lambda_n^{(3)}$....

PCA allows the pair distribution to be expressed as a sum over different modes given by,

$$V_{n\Delta}(\eta_1, \eta_2) \approx \sum_{\alpha=1}^{k} V_n^{(\alpha)}(\eta_1) V_n^{(\alpha)*}(\eta_2), \tag{4.10}$$

where each term corresponds to a different mode of fluctuation.

Comparing Eq. (4.9) and Eq. (4.10), we get

$$V_n^{(\alpha)}(\eta) \equiv \sqrt{\lambda_n}\psi_n^{(\alpha)}(\eta), \tag{4.11}$$

which confirms that eigenvalues should be positive. The normalized definition of flow coefficient is that

$$v_n^{(\alpha)}(\eta) \equiv \frac{V_n^{(\alpha)}(\eta)}{M(\eta)}. \tag{4.12}$$

The fluctuation in multiplicity is described by the quantity $v_0^{(\alpha)}(\eta)$, and $v_n^{(\alpha)}(\eta)$, where $n > 0$, describes the fluctuation in anisotropic flow.

4.3 Principal components of flow fluctuations

To understand the fluctuations in the anisotropic flow coefficients in the longitudinal direction, two-particle correlation matrix is constructed. PCA is performed on the two-particle correlation matrix to extract the leading and significant sub-leading flow modes. We analyze 10^3 Pb+Pb collision events at $\sqrt{s_{NN}} = 5.02$ TeV in the 0 to 1% centrality bin. Initial conditions are generated by T_RENTo 3D with event-by-event fluctuations and hydrodynamical simulation is done with $MUSIC$ which includes non-flow effects such as resonance decays.

4.3.1 Results

The two-particle correlation matrix is constructed in pseudorapidity window ranging from -3 to 3 with 12 bins each of width 0.5. The 12×12 matrix is diagonalized to find eigenvalues and corresponding eigenvectors for PCA. PCA enables us to differentiate the leading and sub-leading modes of fluctuations in the anisotropic flow coefficients in the longitudinal direction which is shown in Fig. (4.3) and sub-leading modes are shown clearly in Fig. (4.4). The eigenvalues for the two-particle correlation matrix $V_{n\Delta}(\eta_1, \eta_2)$ for $n = 0, 2, 3$ and 4 are shown in Table 4.1.

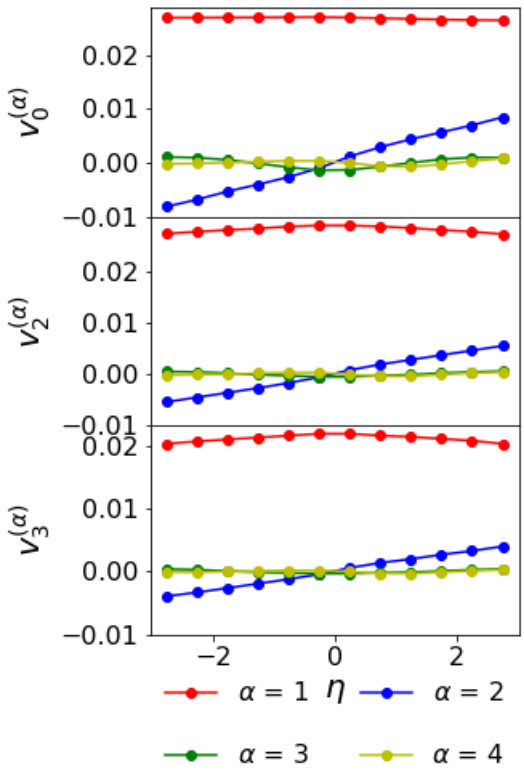

Figure 4.3: Leading and sub-leading modes measured using PCA.

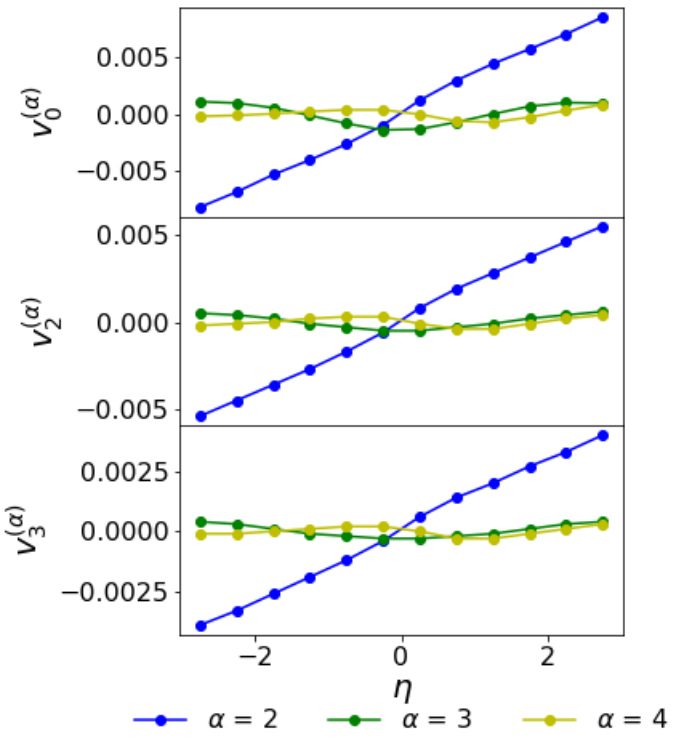

Figure 4.4: Sub-leading modes measured using PCA.

	$\lambda_n^{(1)}$	$\lambda_n^{(2)}$	$\lambda_n^{(3)}$	$\lambda_n^{(4)}$
$n = 0$	34986	1291	38	8
$n = 2$	38484	553	6	3
$n = 3$	21735	293	3	1
$n = 4$	7301	98	1	0.6

Table 4.1: Eigenvalues of PCA.

4.3.2 Discussion

Multiplicity and flow fluctuations as a function of pseudorapidity are shown where α denotes the different modes of fluctuations. The leading mode is $\alpha = 1$ with the largest eigenvalue. The prominent sub-leading modes are $\alpha = 2, 3$ and 4 with successively decreasing eigenvalues. The leading mode, $v_0^{(1)}$ for multiplicity fluctuation, $n = 0$ is 0.03 approximately independent of η. This shows that the events in 0 to 1% centrality bin have a relative multiplicity fluctuation of 3%. Multiplicity fluctuations of events in 0 to 10% centrality bin were found to be about 12% [18]. The deviation of this value obtained in the present work can be attributed to the smaller width of centrality range.

The first sub-leading mode, $v_0^{(2)}$ is smaller than the leading mode and goes from negative to positive values as the value of η goes from negative to positive values. Its eigenvalue $\lambda_0^{(2)}$ is smaller than $\lambda_0^{(1)}$ by a factor of 27. The parity change is due to the asymmetry of the multiplicity in the forward and backward pseudorapidity directions. This is in fact due to the small changes in the nuclear density distribution of the two colliding nuclei because of the event-by-event fluctuation. The next sub-leading modes, $\alpha = 3$ and $\alpha = 4$ also have alternating parities. Basically, $v_n^{(\alpha)}(\eta)$ has $\alpha - 1$ nodes. The eigenvalues decrease again for these modes, $\lambda_0^{(3)} \approx \lambda_0^{(2)}/33$ and $\lambda_0^{(4)} \approx \lambda_0^{(3)}/5$. It is also visible from the figure that modes are orthogonal to each other as is evident from the definition of principal components.

$$\sum_{\alpha=1}^{k} V_n^{(\alpha)}(\eta_1) V_n^{(\beta)*}(\eta_2) = 0, \quad \alpha \neq \beta \tag{4.13}$$

The leading and sub-leading principal components of anisotropic flow for $n = 2, 3$ and 4 are also shown. The leading modes, $v_n^{(1)}$ agree well with the experimental values of flow harmonics, v_n and also depend weakly on η with a small enhancement at mid-rapidity, $\eta = 0$. They represent the hydrodynamic response to initial state eccentricities. The oscillating parity is also visible for principal components of anisotropic flow fluctuations. This behaviour can be explained by relative angle difference in the event plane of the two colliding nuclei. The eigenvalue of leading mode is larger than that of sub-leading mode for the flow harmonics as well. The trend is followed for the subsequent modes also, $\lambda_n^{(2)} \approx \lambda_n^{(1)}/70$, $\lambda_n^{(3)} \approx \lambda_n^{(2)}/95$ and $\lambda_n^{(4)} \approx \lambda_n^{(3)}/2$. The major cause of breaking of factorization (explained in sec. 6.2) is the existence of sub-leading modes which arise due to the initial state fluctuations in the system.

Chapter 5

Method to reduce short-range non-flow effects

The two-particle correlation matrix $V_{n\Delta}(\eta_1, \eta_2)$ in general includes the contribution from both flow and non-flow effects. The second term on the RHS of Eq. (4.8) removes self-correlations in the correlation matrix which is one of the major non-flow contributions. But particles emitted from nearby bins can cause short-range non-flow correlations. This effect can be reduced if we introduce a suitable pseudorapidity gap when measuring two-particle correlation. If we eliminate the elements of the two particle correlation matrix with $\eta_1 \approx \eta_2$ and perform principal component analysis, the non-flow effects in the modes of fluctuations will be much reduced.

5.1 Fixed gap and Mobile gap

The pseudorapidity gap can be imposed in the two-particle correlation matrix in two ways: fixed gap and mobile gap. Pseudrorapidity ranges from -3 to 3 in 12 bins with a bin width of 0.5. In the method of fixed gap, a particular pseudorapidity gap, $|\Delta\eta| > 2$ is imposed by fixing the pseudorapidity gap from -1 to 1 and ignoring all the correlation matrix elements which are constructed using combinations of pseudorapidity bins, within the gap as well as of the same sign. It is shown in Fig. (5.1). The figure is a 12×12 matrix where each block corresponds to the element in the matrix. The blue colored blocks in the matrix denote the

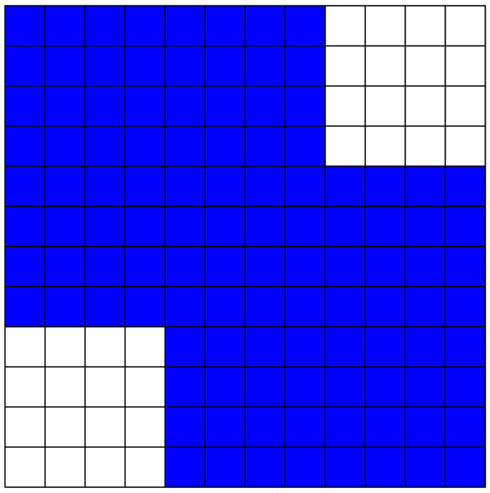

Figure 5.1: Fixed gap

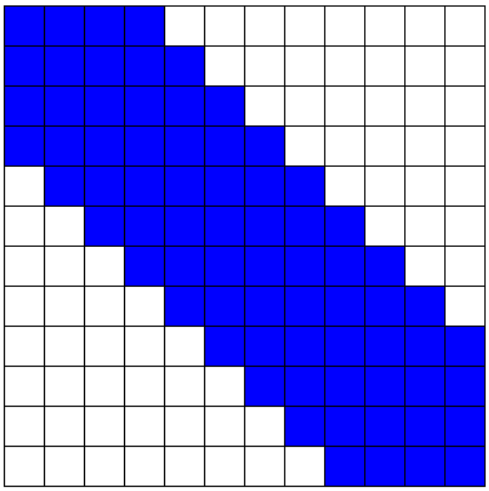

Figure 5.2: Mobile gap

eliminated elements.

The procedure of mobile gap is shown in Fig. (5.2). Here, all the correlation matrix elements with the pseudorapidity difference less than or equal to 2 are ignored. This comparison in the case of pseudorapidity gap $|\Delta\eta| > 2$ shows that the method of mobile gap is more efficient than that of fixed gap since it serves the same purpose by eliminating a smaller number of matrix elements. Therefore, we choose the method of mobile gap in imposing pseudorapidity gaps in correlation matrix.

The primary short range effect comes from interaction of particles from the same bin. So the first step to eliminate such effects is to ignore the diagonal elements where the correlation of each bin is measured with itself. The short range effects from nearby bins can be eliminated by ignoring the elements sitting next to the diagonal elements. This gap can be extended such that most of the short-range non-flow contributions are reduced.

A mobile gap $|\Delta\eta| > 0.5$ indicates the elimination of diagonal elements. Ignoring diagonal and next-to-diagonal elements indicates the imposition of a mobile gap $|\Delta\eta| > 1$. Finally diagonal, next-to-diagonal and next-to-next-to-diagonal elements are dropped indicating that a mobile gap of $|\Delta\eta| > 1.5$ is imposed. After imposing the above mentioned pseudorapidity gaps, PCA is performed and the different modes of flow fluctuations are analyzed.

5.2 PCA with fixed pseudorapidity gap

The two-particle correlation matrix is a 12×12 real and symmetric matrix. There are only 78 independent elements instead of 144, since it is a symmetric matrix. If we assume the matrix has one significant eigenvalue and others are negligible, the eigenvector can be constructed demanding that $|eigenvector\rangle\langle eigenvector|$ yields the matrix. The number of independent elements denoted by N_{indep} will vary depending on the pseudorapidity gap imposed on the correlation matrix. For example, if we are imposing a pseudorapidity gap of $|\Delta\eta| > 0.5$, diagonal elements have to be ignored, resulting in 66 independent elements. The number of independent elements corresponding to different pseudorapidity gaps are shown in table 5.1.

	Change in the matrix	$\lvert\Delta\eta\rvert$	N_{indep}
(a)	No elements dropped	$\lvert\Delta\eta\rvert \geq 0$	78
(b)	D dropped	$\lvert\Delta\eta\rvert > 0.5$	66
(c)	D and D $\pm$ 1 dropped	$\lvert\Delta\eta\rvert > 1.0$	55
(d)	D, D $\pm$ 1 and D $\pm$ 2 dropped	$\lvert\Delta\eta\rvert > 1.5$	45

Table 5.1: Independent elements of correlation matrix with pseudorapidity gaps.

We are interested in exploring the leading and the first two sub-leading modes of the pseudorapidity gaps imposed correlation marix obtained on performing PCA. The leading mode is analyzed by the method of one-mode fit. This method is also called 12-parameter fit since the leading mode has 12 parameters. The idea is to reproduce all the independent elements in the matrix by only using the information of 12 parameters. Similarly, in the method of 2-mode fit or 24-parameter fit, the leading and the first sub-leading mode which has 24 parameters in total reproduce all the independent elements in the matrix. The fit values are found using a method called direction set (Powell's) methods in multidimensions [21]. The number of free elements, N_{free} is defined as $N_{free} = N_{indep} - N_{para}$ which is shown in Table 5.2.

In the Powell's method, a function of n variables is minimized starting from a vector in $n-$dimensions towards a particular direction. Input consists of a vector in $n-$dimensions and a matrix with dimensions $n \times n$ whose columns contain the initial set of directions for the given vector to optimize. In our case, the input vector is eigenvector which has 12

	N_{indep}	1 mode fit $N_{para} = 12$	2 mode fit $N_{para} = 24$	3 mode fit $N_{para} = 36$
(a)	78	66	54	42
(b)	66	54	42	30
(c)	55	43	31	19
(d)	45	33	21	9

Table 5.2: Free elements of correlation matrix with pseudorapidity gaps.

components, the function is χ^2 which is the function of 12 components of the eigenvector and the input matrix is 12×12 correlation matrix with the number of independent elements depends on the pseudorapidity gap imposed. After many iterations, the output is the best fit of eigenvector with the minimized χ^2. The correlation matrix is the direction set of the final iteration. By diagonalizing the matrix, eigenvalues and eigenvectors correponding to different modes of flow fluctuation are found and compared with that of the original matrix where no elements are ignored.

The goodness of fit can be well tested using χ^2 analysis [22]. In this method, the weighted sum of squares of the deviation of the data from the fitting function is minimized to describe the data in a best way. χ^2 is defined as,

$$\chi^2 \equiv \sum_{1}^{N_{indep}} \left\{ \frac{1}{\sigma_i^2} [y_i - y(x_i)]^2 \right\}, \tag{5.1}$$

where y_i's are the data points, $y(x_i)$ is the fitting function, and σ_i^2 denotes the variance in the data point y_i. Reduced chi-square, χ^2_{red} is defined as the ratio of χ^2 to the number of degrees of freedom.

$$\chi^2_{red} \equiv \frac{\chi^2}{N_{free}}. \tag{5.2}$$

The best fit results in a value of $\chi^2_{red} = 1$. If the fitting function does not describe the data very well, χ^2_{red} will be very much larger than 1. The value of $\chi^2_{red} \ll 1$ describes an error in the assignment of uncertainties in the measured variables.

The variance of the data, σ^2 is calculated using the Jackknife method [23]. It is a resampling technique used to determine standard deviation for a set of measurements. Suppose we have a set of n observations: $x_1, x_2, .., x_n$ and an estimator, $\hat{X}$. We construct

samples eliminating single observation at a time: $x_{(i)} = x_1, x_2, .., x_{i-1}, x_{i+1}.., x_n$. $\hat{X}_{(i)}$ denotes the estimate calculated leaving the i^{th} observation. Jackknife estimate of variance is defined as,

$$\sigma^2 = \frac{n-1}{n}\sum_{i=1}^{n}(\hat{X}_{(i)} - \hat{X})^2, \tag{5.3}$$

where $\hat{X}$ denotes the estimate including all the sample points. This method works well when the estimator is linear (eg: mean).

The quantity that we are interested in is the correlation coefficient which is a non-linear statistical measure. In that case, we divide the data into M blocks with a significant block length. We construct the correlation coefficient eliminating one block at a time. $\hat{X}_{(m)}$ denotes the estimate calculated leaving the m^{th} block. The variance is defined as,

$$\sigma^2 = \frac{M-1}{M}\sum_{i=1}^{M}(\hat{X}_{(m)} - \hat{X})^2, \tag{5.4}$$

where $\hat{X}$ denotes the correlation coefficient with all the blocks.

Tables (5.3), (5.5) and (5.7) shows the eigenvalues and χ^2_{red} values for the one-mode, two-mode and three-mode fits for elliptic flow correlation matrix, $V_{n\Delta}(\eta_1, \eta_2)$ respectively. The column 1 notation corresponds to the four different cases mentioned in Table (5.1). The first two leading eigenvalues of the two-particle correlation matrix without any pseudorapidity gaps for elliptic flow ($n = 2$) are 38484 and 553 and that of triangular flow ($n = 3$) are 21735, and 283. The eigenvalues in the case of one-mode and two-mode fits are consistent with the largest two eigenvalues of the original two-particle correlation matrix. This trend is visible in the case of triangular flow also ($n = 3$) shown in Table (5.4), (5.6) and (5.8). This indicates the leading and the first sub-leading mode are clearly visible even when short-range non-flow effects are removed.

The values of χ^2_{red} which are close to 1 show the better fit. Also, χ^2_{red} is close to 1 when the difference between number of parameters N_{para} and number of independent elements N_{indep} is small. Since this difference is large in the case of 12-parameter fit, the large values of χ^2_{red} are justified.

1 mode or 12-parameter fit	χ^2_{red}	λ_1
(a)	13.1	38353
(b)	10.8	38303
(c)	7.8	38268
(d)	4.4	38296

Table 5.3: One-mode fit for $n = 2$

1 mode or 12-parameter fit	χ^2_{red}	λ_1
(a)	7.9	21709
(b)	7.6	21673
(c)	6.3	21644
(d)	3.7	21615

Table 5.4: One-mode fit for $n = 3$

2 mode or 24-parameter fit	χ^2_{red}	λ_1	λ_2
(a)	1.2	38481	565
(b)	1.4	38462	617
(c)	1.1	38453	566
(d)	1.1	38458	728

Table 5.5: Two-mode fit for $n = 2$

2 mode or 24-parameter fit	χ^2_{red}	λ_1	λ_2
(a)	3.6	21526	464
(b)	2.9	21541	491
(c)	1.9	21564	547
(d)	1.0	21583	513

Table 5.6: Two-mode fit for $n = 3$

3 mode or 36-para fit	χ^2_{red}	λ_1	λ_2	λ_3
(a)	1.2	38433	454	97
(b)	1.1	38447	533	106
(c)	0.5	38436	634	105
(d)	1.7	38458	719	195

Table 5.7: Three-mode fit for $n = 2$

3 mode or 36-para fit	χ^2_{red}	λ_1	λ_2	λ_3
(a)	1.1	21607	370	68
(b)	0.6	21625	332	178
(c)	1.7	21611	393	149
(d)	1.3	21621	259	98

Table 5.8: Three-mode fit for $n = 3$

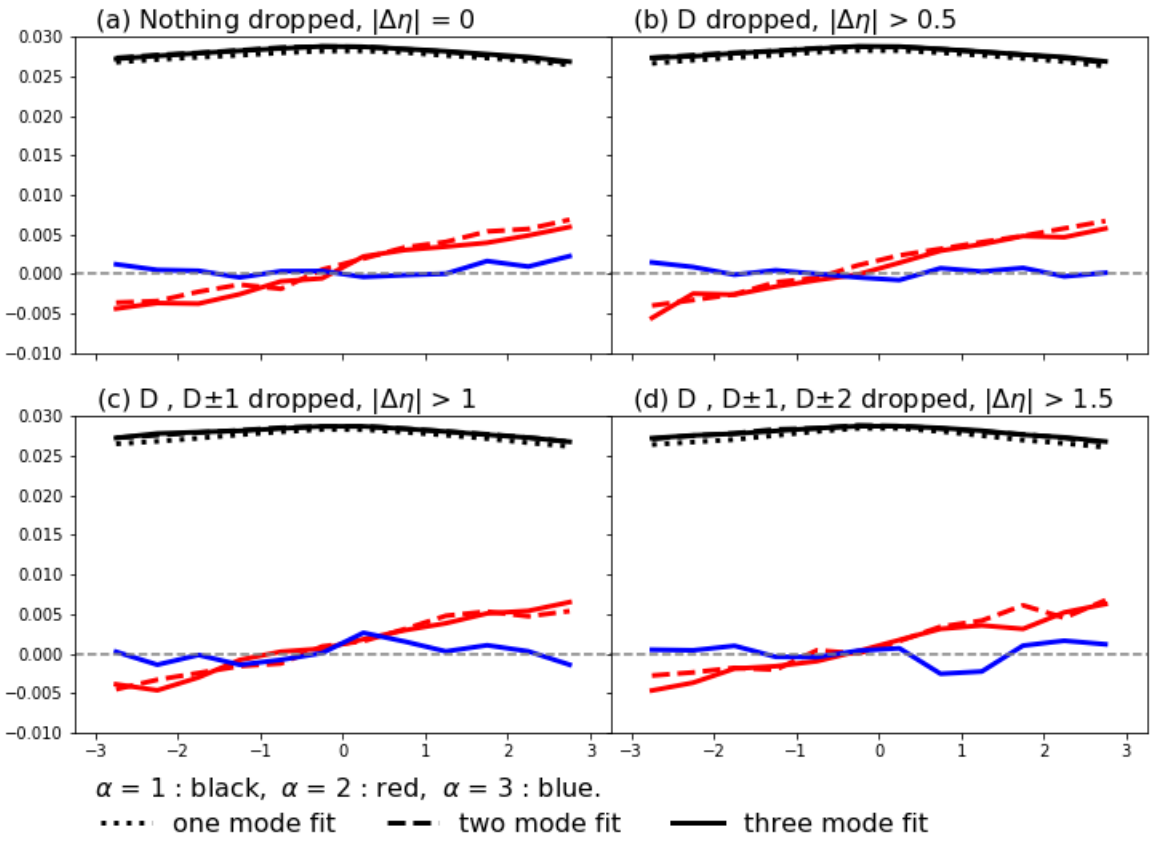

Figure 5.3: Elliptic flow modes

5.3 Flow modes

PCA is performed on the two-particle correlation matrix with pseudorapidity gaps, $|\Delta\eta| > 0.5$, $|\Delta\eta| > 1$ and $|\Delta\eta| > 1.5$. Figure. (5.3) shows the different modes of elliptic flow fluctuation and Fig. (5.4) shows the different modes of triangular flow fluctuations.

The figure shows that even if pseudorapidity gaps are imposed, the first three leading modes are clearly evident and measurable. We have discussed earlier that the leading mode depicts the response of hydrodynamics to the initial geometry. The leading modes are undisturbed by the elimination of elements corresponds to the short-range effects in the correlation matrix. This indicates that the non-flow effects do not contribute significantly to the elliptic flow measured using two-particle correlation. On the other hand, abruptness

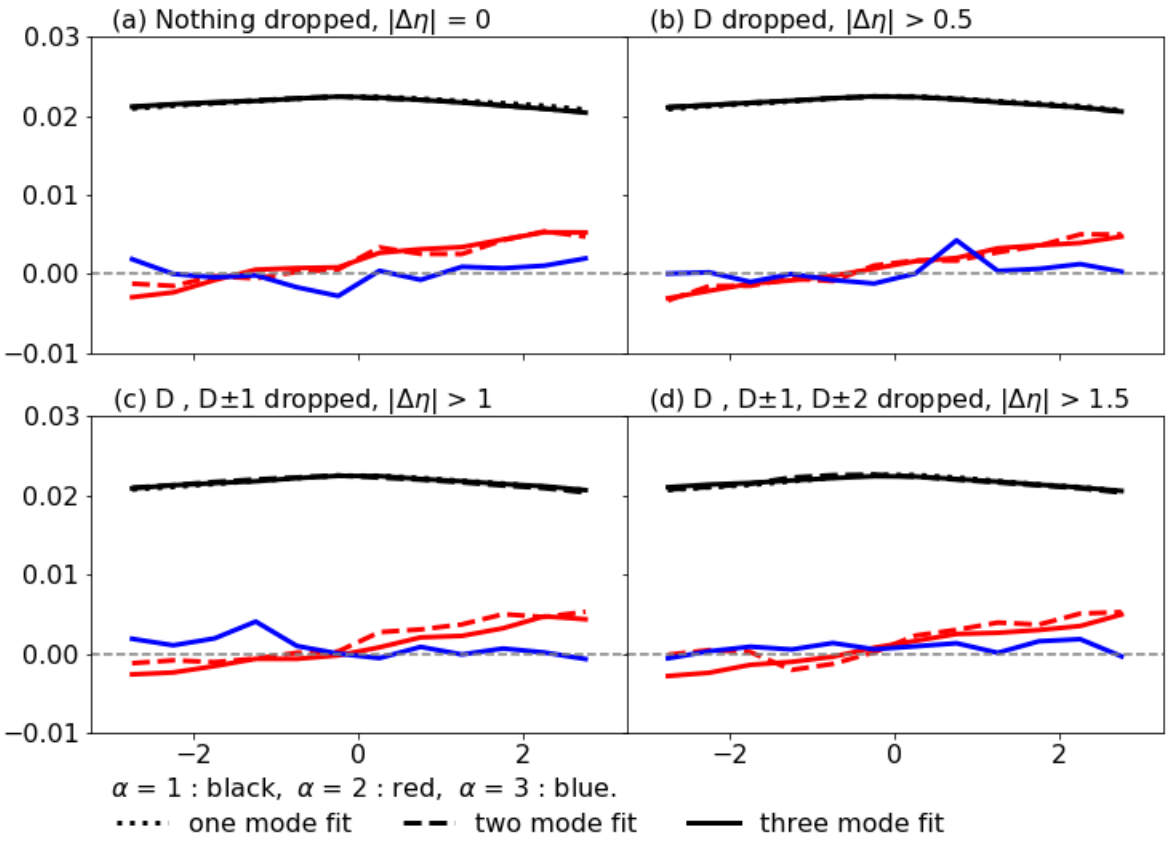

Figure 5.4: Triangular flow modes

in the second sub-leading mode $v_n^{(3)}$ for $n = 2$ and $n = 3$ can suggest that non-flow effects are not completely removed from the system. A parity change is visible in the first sub-leading mode $v_n^{(2)}$ for $n = 2$ and $n = 3$ which indicates the asymmetry of multiplicity in the forward and backward direction. PCA of pseudorapidity dependence of flow fluctuation has not yet been done experimentally. It is evident that sub-leading modes are more sensitive to non-flow effects than is the leading mode.

Chapter 6

Decorrelations of anisotropic flows

Due to event by event fluctuations, magnitude of the flow vector and the flow orientation vary from event to event. Fluctuations can cause measurable decorrelations of anisotropic flow in the pseudorapidity direction. Because of the fluctuation, the magnitude of the flow vector v_n and flow orientation Ψ_n at two different pseudorapidities will be different: $V_n(\eta_1) \neq V_n(\eta_2)$. This phenomenon is also called flow factorization breaking in pseudorapidity as explained in section. 6.2. This quantity provides additional information about the initial state fluctuations. CMS collaboration proposed a reference-rapidity-bin method to study the longitudinal decorrelations of anisotropic flow [24].

6.1 Reference-rapidity-bin method

In this method, the correlation between flow in rapidity bins η and $-\eta$ is measured by constructing a quantity $r[n,k]$ defined as,

$$r[n,k](\eta) = \frac{\langle Q_n^k(-\eta) Q_n^{*k}(\eta_r)\rangle}{\langle Q_n^k(\eta) Q_n^{*k}(\eta_r)\rangle}, \tag{6.1}$$

where Q_n is the Q-vector defined in Eq. 4.7 and η_r is the reference rapidity bin. We are interested in $k = 1$ only. We choose the rapidity bins, $\pm\eta$ in the interval -2.5 to 2.5 and the reference rapidity window in the forward direction $2.5 < \eta_r < 3.0$. As the rapidity gap between $-\eta$ and η_r increases, the short-range non-flow effects become small. The quantity

$r[n,k]$ measures the decorrelation between η and $-\eta$ by comparing it with reference rapidity bin η_r. Hence, this is also called three-rapidity bin method.

In order to have a deeper understanding, two other decorrelation functions are also constructed to analyze the decorrelation of the flow magnitude v_n and flow orientation Ψ_n specifically [25]. Longitudinal decorrelation of flow magnitude v_n is defined as,

$$r_M[n,k](\eta) = \frac{\langle q_n^k(-\eta) q_n^{*k}(\eta_r)\rangle}{\langle q_n^k(\eta) q_n^{*k}(\eta_r)\rangle}, \tag{6.2}$$

where q_n is the magnitude of vector Q_n. The longitudinal decorrelation of flow orientation is defined as,

$$r_\Psi[n,k](\eta) = \frac{\langle \hat{Q}_n^k(-\eta) \hat{Q}_n^{*k}(\eta_r)\rangle}{\langle \hat{Q}_n^k(\eta) \hat{Q}_n^{*k}(\eta_r)\rangle}, \tag{6.3}$$

where $\hat{Q}_n$ is defined as Q_n/q_n.

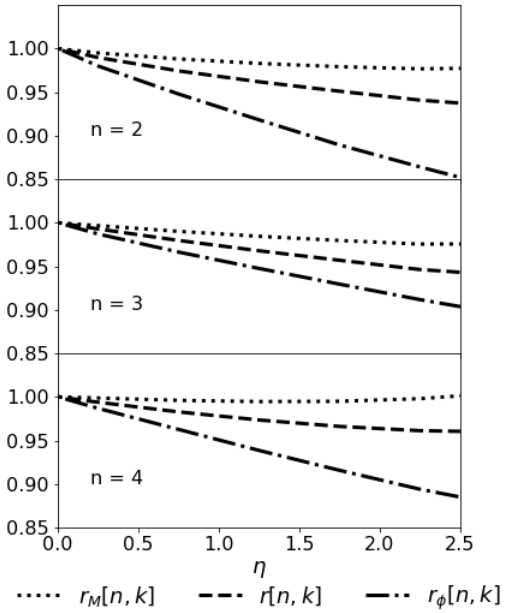

Figure 6.1: Decorrelation functions $r[n,1]$, $r_M[n,1]$ and $r_\Psi[n,1]$ with $n = 2, 3$ and 4

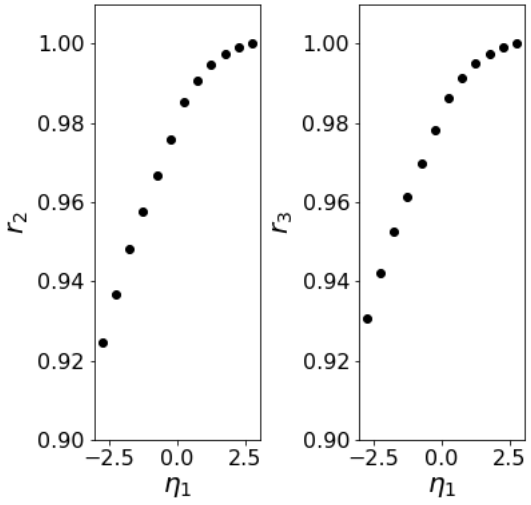

Figure 6.2: Ratio of correlation between diagonal and non-diagonal elements.

.

We analyze 10^3 Pb+Pb collisions at $\sqrt{s_{NN}} = 5.02$ TeV in the centrality range 0 to 1%. In Fig. 6.1, the longitudinal decorrelation functions $r[n,1]$, $r_M[n,1]$ and $r_\Psi[n,1]$ for flow harmonics $n = 2, 3$ and 4 are shown. The fully fluctuating initial density profile is taken from T_RENTo 3D and hydrodynamic simulations are perfomed using $MUSIC$. The rapidity bins are taken in mid-rapidity from -2.5 to 2.5 and reference rapidity window is taken as $2.5 < \eta_r < 3.0$.

The interesting feature of all the decorrelations functions is that it is clearly linear in the mid-rapidity range for the anisotropic flow coefficients, v_2, v_3 and v_4. As the gap between the pseudorapidity bins increases, correlation between flow coefficients decreases, thereby non-flow effects are reduced. We can see the slopes of the three curves follow a trend. The slope of flow orientation, r_Ψ is always higher than that of the flow magnitude r_M and the flow vector r. This clearly indicates that flow orientation is much more sensitive to the longitudinal fluctuations in the initial state. The flow magnitudes are almost independent of flow fluctuations. The flow vector sits in between the flow magnitude and the flow orientation because the flow vector represents the combined sensitivity of both flow magnitude and flow orientation to the initial-state fluctuations in the longitudinal direction.

6.2 Decorrelation in breaking of factorization

As explained in Eq. (3.20), when we are neglecting contribution non-flow components, we should be able to factorize two-particle correlation as product of two single particle distribution functions. This has been tested on particle-pairs in different bins of transverse momentum [26]. They found that,

$$V_{n\Delta}(p_a, p_b) = V_n^{(\alpha)}(p_a) V_n^{(\alpha)*}(p_b), \tag{6.4}$$

where p_a and p_b correspond to two different transverse momentum bins. This relation cannot hold true when non-flow effects are present. So this relation is non-trivial observation coming from the fact that particles are emitted independently at the end of the hydrodynamical expansion.

In Eq. (4.10), breakdown from factorization is shown. This does not mean that hydrodynamical picture is breaking. Instead, this is a consequence of event-by-event

fluctuation present in the initial state of the heavy-ion collision even in the hydrodynamic system [27].

The event-averaged correlation matrix obeys the following two conditions.
1) Diagonal elements must be positive:

$$V_{n\Delta}(p^a, p^a) \geq 0 \tag{6.5}$$

2) The matrix obeys Cauchy-Schwarz inequality:

$$V_{n\Delta}(p^a, p^b)^2 \leq V_{n\Delta}(p^a, p^a) V_{n\Delta}(p^b, p^b) \tag{6.6}$$

It is clear from the Cauchy-Schwarz inequality that flow does not imply factorization. Violation of the above two properties indicates the presence of non-flow.

The validity of the Cauchy-Schwarz inequality is tested on 1000 Pb+Pb collision events at 5.02 TeV from 0-1% centrality bin by constructing a parameter r_n which is defined as,

$$r_n = \frac{V_{n\Delta}(\eta^a, \eta^b)}{\sqrt{V_{n\Delta}(\eta^a, \eta^a) V_{n\Delta}(\eta^b, \eta^b)}}. \tag{6.7}$$

Here, r_n is a correlator which measures the decorrelation of flow at two pseudorapidity bins. According to the inequality, r_n should lie between -1 and 1. If $r_n = 1$, it implies the saturation condition where factorization is present. Figure. (6.2) shows r_n where $n = 2, 3$ as a function of η_1 where η_2 is fixed at -2.75 and η_1 varies from -2.75 to 2.75 in 12 bins.

Factorization breaking is visible in elliptic and triangular flows. And this breaking increases with the difference $|\eta_1 - \eta_2|$. r_n is non-negative and always less than 1. This confirms that non-flow effects are absent.

Chapter 7

Conclusion

In this thesis, we have presented a new method to study the event-by-event fluctuation in the longitudinal direction of relativistic heavy-ion collisions. We used the initial condition model T_RENTo 3D to generate fully fluctuating initial profiles and the 3+1 D viscous hydrodynamic model $MUSIC$ to perform hydrodynamic simulation. It is known that the fluctuations in the initial state will leave their signature on the hadronic observables. One such interesting hadronic observable is anisotropic flow coefficients. The hydrodynamic expansion converts the spatial anisotropies in the initial state of QGP to momentum anisotropies which is represented by anisotropic flow coefficients. The method of principal component analysis is applied to the correlation matrix in which each element represents the correlation between flow coefficients in two different pseudorapidity bins.

PCA fully exploits all the information contained in the two-particle correlation matrix to analyze the flow fluctuations. 10^3 Pb+Pb collision events at $\sqrt{s_{NN}} = 5.02$ TeV in the centrality range 0 to 1% are analyzed using PCA which revealed the dominant modes of the flow. The leading modes constructed from two-particle correlation matrix are the same as experimentally measured anisotropic flow coefficients. Therefore the leading modes represent the hydrodynamic response to initial state eccentricities. The sub-leading modes basically come from the event-by-event initial-state fluctuations which are responsible for the breaking of factorization. Multiplicity and flow fluctuations in the entire sample of events are represented by four principal components since the higher modes are negligible.

A new method is presented which eliminates the short-range non-flow effects from the

anisotropic flow. A suitable pseudorapidity gap is imposed on the two-particle correlation matrix and the flow modes are studied. We found that even if a pseudorapidty gap $|\Delta\eta| > 1.5$ is imposed, the first two sub-leading modes are clearly measurable. The method also shows that sub-leading modes are more sensitive to the non-flow effects than are the leading modes. In addition, we also studied the longitudinal decorrelation of flow vectors, flow magnitudes and flow orientations. We found that flow orientation is much more sensitive to the decorrelation effects than the flow magnitude.

Bibliography

[1] Kolb, Peter F., and Ulrich Heinz. "Hydrodynamic description of ultrarelativistic heavy-ion collisions." QuarkGluon Plasma 3. 2004. 634-714.

[2] Shen, Chun, and Ulrich Heinz. "The road to precision: Extraction of the specific shear viscosity of the quark-gluon plasma." Nuclear Physics News 25.2 (2015): 6-11.

[3] Alver, B., et al. "Importance of correlations and fluctuations on the initial source eccentricity in high-energy nucleus-nucleus collisions." Physical Review C 77.1 (2008): 014906.

[4] Moreland, J. Scott, Jonah E. Bernhard, and Steffen A. Bass. "Alternative ansatz to wounded nucleon and binary collision scaling in high-energy nuclear collisions." Physical Review C 92.1 (2015): 011901.

[5] Ke, W., Moreland, J. S., Bernhard, J. E., and Bass, S. A. (2017). "Constraints on rapidity-dependent initial conditions from charged-particle pseudorapidity densities and two-particle correlations." Physical Review C, 96(4), 044912.

[6] Schenke, Bjoern, Sangyong Jeon, and Charles Gale. "(3+ 1) D hydrodynamic simulation of relativistic heavy-ion collisions." Physical Review C 82.1 (2010): 014903.

[7] Tuchin, Kirill. "Particle production in strong electromagnetic fields in relativistic heavy-ion collisions." Advances in High Energy Physics 2013 (2013).

[8] Huovinen, Pasi, and Pter Petreczky. "QCD equation of state and hadron resonance gas." Nuclear Physics A 837.1-2 (2010): 26-53.

[9] Rafelski, Johann. "Melting hadrons, boiling quarks." Eur. Phys. J. A 51.arXiv: 1508.03260 (2015): 114.

[10] Huovinen, Pasi, and Hannah Petersen. "Particlization in hybrid models." The European Physical Journal A 48.11 (2012): 171.

[11] Cooper, Fred. "F. Cooper and G. Frye, Phys. Rev. D 10, 186 (1974)." Phys. Rev. D 10 (1974): 186.

[12] Qiu, Zhi, and Ulrich Heinz. "Event-by-event shape and flow fluctuations of relativistic heavy-ion collision fireballs." Physical Review C 84.2 (2011): 024911.

[13] Bhalerao, R. S. "Collective flow in relativistic heavy-ion collisions." Pramana 61.5 (2003): 1021-1025.

[14] Luzum, Matthew. "Flow fluctuations and long-range correlations: elliptic flow and beyond." Journal of Physics G: Nuclear and Particle Physics 38.12 (2011): 124026.

[15] Aaboud, Morad, et al. "Measurement of the azimuthal anisotropy of charged particles produced in $\sqrt{s_{NN}}$ = 5.02 TeV Pb+ Pb collisions with the ATLAS detector." The European Physical Journal C 78.12 (2018): 997.

[16] Chatrchyan, Serguei, et al. "Centrality dependence of dihadron correlations and azimuthal anisotropy harmonics in PbPb collisions at $\sqrt{s_{NN}}$ = 2.76 TeV." The European Physical Journal C 72.5 (2012).

[17] Luzum, Matthew, and Hannah Petersen. "Initial state fluctuations and final state correlations in relativistic heavy-ion collisions." Journal of Physics G: Nuclear and Particle Physics 41.6 (2014): 063102.

[18] Bhalerao, Rajeev S., et al. "Principal component analysis of event-by-event fluctuations." Physical review letters 114.15 (2015): 152301.

[19] Jolliffe, Ian. Principal component analysis. Springer Berlin Heidelberg, 2011.

[20] Poskanzer, Arthur M., and Sergei A. Voloshin. "Methods for analyzing anisotropic flow in relativistic nuclear collisions." Physical Review C 58.3 (1998): 1671.

[21] Press, William H., et al. Numerical recipes in Fortran 90. Vol. 2. Cambridge: Cambridge university press, 1996.

[22] Bevington, Philip R., et al. "Data reduction and error analysis for the physical sciences." Computers in Physics 7.4 (1993): 415-416.

[23] Miller, Rupert G. "The jackknife-a review." Biometrika 61.1 (1974): 1-15.

[24] Khachatryan, Vardan, et al. "Evidence for transverse-momentum-and pseudorapidity-dependent event-plane fluctuations in PbPb and p Pb collisions." Physical Review C 92.3 (2015): 034911.

[25] Pang, Long-Gang, et al. "Longitudinal fluctuations and decorrelation of anisotropic flow." Nuclear Physics A 956 (2016): 272-275.

[26] Aamodt, K., et al. "Harmonic decomposition of two particle angular correlations in PbPb collisions at $\sqrt{s_{NN}}$ = 2.76 TeV." Physics Letters B 708.3-5 (2012): 249-264.

[27] Gardim, Fernando G., et al. "Breaking of factorization of two-particle correlations in hydrodynamics." Physical Review C 87.3 (2013): 031901.